Measurement of $\mathbf{BR(K_S \rightarrow \pi^{\pm} e^{\mp} \nu_e)}$ and $\mathbf{\Delta m = m_{K_L} - m_{K_S}}$ in $\mathbf{K_{S,L} \rightarrow \pi^{\pm} e^{\mp} \nu_e}$ Decays.

Trabajo de Investigación
de
Cristina Morales

Valencia, Septiembre de 2002

Facultad de Física
Universidad de Valencia

Dra. CARMEN GARCÍA GARCÍA, Científico titular del C.S.I.C.

CERTIFICA:

Que la presente memoria "Measurement of BR($K_S \rightarrow \pi e \nu_e$) and $\Delta m = m_{K_L} - m_{K_S}$ in $K_{S,L} \rightarrow \pi^{\pm} e^{\mp} \nu_e$ Decays" ha sido realizada bajo mi dirección en el Departamento de Física Atómica, Molecular y Nuclear de la Universidad de Valencia por Dña. Cristina Morales Morales y constituye su trabajo de investigación.

Y para que conste, en cumplimiento de la legislación vigente, firmo el presente Certificado en Burjasot a 10 de septiembre de 2002.

Carmen García García

A Sol,

Prefacio

Como consecuencia del teorema CPT y la regla $\Delta S = \Delta Q$, la anchura de desintegración semileptónica de los mesones K_S y K_L debe ser idéntica. Mientras que las desintegraciones $K_L \to \pi^{\pm} e^{\mp} \nu_e$ y $K_L \to \pi^{\pm} \mu^{\mp} \nu_{\mu}$ corresponden a casi dos tercios de la anchura total de desintegración del K_L, la probabilidad de la desintegración $K_S \to \pi^{\pm} e^{\mp} \nu_e$ fue medida por primera vez en los últimos años como resultado de la reacción $e^+ e^- \to \phi(1020) \to K_L K_S$ [1, 2]. De esta reacción es posible obtener una muestra limpia de mesones K_S mediante la identificación de los K_L que se producen en la desintegración de la resonancia ϕ intermedia.

En el NA48 el mecanismo de producción de los mesones K_S y K_L es completamente diferente ya que se crean K^0 y $\overline{K^0}$ a partir de colisiones protón-Nucleón. Los estados K_S y K_L son combinaciones lineales de K^0 y $\overline{K^0}$ y son los estados que se desintegran bajo interacción débil.

Despreciando violación de CP es posible escribir la intensidad de desintegración en los dos estados semielectrónicos de carga en función de la vida media t como

$$N_{K \to \pi^{\mp} e^{\pm} \nu_e}(t) \quad \propto \quad \eta^2 e^{-\Gamma_S t} + e^{-\Gamma_L t} \pm 2\ \eta\ \frac{N_{K^0} - N_{\overline{K^0}}}{N_{K^0} + N_{\overline{K^0}}}\ e^{-\frac{1}{2}(\Gamma_L + \Gamma_S) t} \cdot cos(\Delta m \cdot t),$$

donde $\Delta m = m_{K_L} - m_{K_S}$ y $\eta = \langle K_S | \mathrm{H} | \pi^{\pm} e^{\mp} \nu_e \rangle / \langle K_L | \mathrm{H} | \pi^{\pm} \mathrm{e}^{\mp} \nu_{\mathrm{e}} \rangle$ y donde se observa la contribución de una componente de desintegración rápida correspondiente a los K_S, una componente de desintegración lenta correspondiente a los K_L y la interferencia de $K_S K_L$.

Con los datos tomados durante el período de alta intensidad de K_S de septiembre del año 1999, el llamado "1999 K_S High Intensity Run", fue posible medir estas distribuciones. Aproximadamente 100000 eventos correspondientes a desintegraciones semielectrónicas de K_S y K_L fueron encontrados. Un ajuste de las distribuciones de desintegración hizo posible la medida de Δm y BR($K_S \to \pi^{\pm} e^{\mp} \nu_e$).

Los resultados que se presentan en este trabajo son:

$$\begin{aligned}\Delta m &= (0.443 \pm 0.039\ _{\text{(stat)}}\ {}^{+0.011}_{-0.021}\ _{\text{(syst)}})\ \hbar\tau_S^{-1},\\ \mathrm{BR}(K_S \to \pi^\pm e^\mp \nu_e) &= (5.31 \pm 0.46\ _{\text{(stat)}}\ {}^{+0.98}_{-0.71}\ _{\text{(syst)}}) \times 10^{-4}.\end{aligned}$$

De la toma de datos del verano de 2002 se espera obtener una estadística entre 600 - 800 veces superior a la de septiembre de 1999 para las desintegraciones semielectrónicas del K_S. De esta manera será posible un estudio más detallado de la $\mathrm{BR}(\mathrm{K_S} \to \pi^\pm \mathrm{e}^\mp \nu_\mathrm{e})$ así como del llamado "dilution factor" $D(p) = \frac{N_{K^0} - N_{\overline{K^0}}}{N_{K^0} + N_{\overline{K^0}}}$.

Contents

1 Introduction

1.1 The Standard Model

A 'Standard Model' is a theoretical framework built from observation that predicts and correlates new data. Like its precursors in other fields, the Standard Model (SM) of particle physics has been enormously successful in predicting a wide range of phenomena. Its remarkable success strongly suggests that the SM will remain an excellent approximation to nature at distance scales as small as 10^{-18} m.

Particle physicists describe nature in terms of four distinct forces, characterized by widely different ranges and strengths as measured at a typical energy scale of 1 GeV. The strong nuclear force has a range of about 10^{-15} m. The weak force responsible for radioactive decays, with a range of 10^{-17} m, is about 10^{-5} times weaker at low energy. The electromagnetic force that governs much of macroscopic physics has infinite range and strength determined by the fine structure constant, $\alpha \approx 10^{-2}$. The fourth force, gravity, also has infinite range and a low energy coupling (about 10^{-38}) - too weak to be observable in laboratory experiments. The achievement of the SM was the elaboration of a unified description of the strong, weak and electromagnetic forces in the language of quantum field gauge theories. Moreover, the SM combines the weak and electromagnetic forces in a single electroweak gauge theory, reminiscent of Maxwell's unification of seemingly distinct forces of electricity and magnetism.

The SM is characterized in part by the spectrum of elementary fields shown in Table 1. The matter fields are fermions and their anti-particles, with half a unit of intrinsic angular momentum, or spin. There are three families of fermion fields that are identical in every attribute except their masses. The first family includes the up (u) and down (d) quarks that are the constituents of nucleons as well as pions and other hadrons. It also contains the electron and the neutrino emitted with a positron in nuclear β-decays. The quarks of the other families are constituents of heavier short-lived particles; they and their companion charged leptons rapidly decay via the weak force to the quarks and leptons of the first family.

Spin-1 gauge bosons mediate interactions among fermions (see Table 2). The electromagnetic force is well understood as a renormalizable quantum field theory known as quantum electrodynamics or QED. 'Renormalizable' means that once a few parameters are determined by a limited set of measurements, the quantitative features of interactions among charged particles and photons can be calculated to arbitrary accuracy as a perturbative expansion in the fine structure constant. In QED, interactions

	QUARKS:	S = $\frac{1}{2}$	
q = $+\frac{2}{3}$	m	q = $-\frac{1}{3}$	m
u_i	$(1-5)10^{-3}$	d_i	$(3-9)10^{-3}$
c_i	$1.15-1.35$	s_i	$0.075-0.170$
t_i	173.8 ± 5.0	b_i	$4.0-4.4$
	LEPTONS:	S = $\frac{1}{2}$	
q = -1	m	q = 0	m
e	5.11×10^{-4}	ν_e	$< 1.5 \times 10^{-8}$
μ	0.105666	ν_μ	$< 1.7 \times 10^{-5}$
τ	1.7770	ν_τ	$< 1.8 \times 10^{-2}$

Table 1: Elementary particles of the SM I: S ($\hbar$) is the spin, q (e) is the electric charge, and m (GeV/c^2) is the mass. Subscript i can take the three different color states of quarks [3].

among electrically charged particles are due to the exchange of quanta of the electromagnetic field called photons (γ). The fact that the γ is massless accounts for the long range of the electromagnetic force.

The strong force, quantum chromodynamics or QCD, is mediated by the exchange of massless gluons (g) between quarks that carry a quantum number called color. In contrast to the electrically neutral photon, gluons (the quanta of the 'chromo-magnetic' field) possess color charge and hence couple to one another. As a consequence, the color force between two colored particles increases in strength with increasing distance. Thus quarks and gluons cannot appear as free particles, but exist only inside composite particles, called hadrons, with no net color charge. Baryons are composed of three quarks of different colors, resulting in 'white' color-neutral states. Mesons contain quark and antiquark pairs whose color charges cancel. Since a gluon inside a nucleon cannot escape its boundaries, the strong nuclear force is mediated by color-neutral bound states, accounting for its short range, characterized by the Compton wavelength of the lightest of these: the π-meson.

The even shorter range of the weak force is associated with the Compton wave-lengths of the charged W and neutral Z bosons that mediate it. Their couplings to the 'weak charges' of quarks and leptons are comparable in strength to the electromagnetic coupling. As the W particles carry electric charge they must couple to the γ, implying a gauge theory that unites the weak and electromagnetic interactions, similar to QCD in that the gauge particles are self-coupled. In distinction to γ's and gluons, W's couple only to left-handed fermions (with spin oriented opposite to the direction of motion).

GAUGE BOSONS: S = 1		
Interaction	quanta	m
Strong	$g_{1,\ldots 8}$	$<$ a few $\times 10^{-3}$
Electromagnetic	γ	$< 2 \times 10^{-25}$
Weak	$W^{\pm}$, Z^0	$80.43 \pm 0.05, 91.188 \pm 0.002$

Table 2: Elementary particles of the SM II: Numerical subscripts indicate the different color states of gluons and m (GeV/c^2) is the mass [3].

One shortcoming of the SM is its failure to accomodate gravity, for which there is no renormalizable quantum field theory because the quantum of the gravitational field, the graviton, carries two units of spin. Recent theoretical progresses suggest that quantum gravity can be formulated only in terms of extended objects like strings and membranes, with dimensions of the order of the Planck length 10^{-35} m. More information about the Standard Model of Particles Physics can be found in ref [4].

1.2 Symmetry Transformations in Physics

Symmetries play a very important role in physics. They govern the most basic physical laws that are known: conservation laws and the interactions of particles in quantum field theory. Conservation laws are intimately related to symmetries via Noether's theorem. The homogeneity of space and time, reflected by the invariance of physical laws under translations in space and time, has the conservation of momentum and energy as consequence. In the same way, the invariance under rotation is linked to the conservation of angular momentum. In quantum field theory the invariance under a global phase shift of the particle fields $\Psi(x)$ (global gauge invariance)

$$\Psi(x) \rightarrow e^{ig\Phi} \cdot \Psi(x), \tag{1.1}$$

implies the conservation of charge.
In order to make a field theory invariant under local gauge transformations

$$\Psi(x) \rightarrow e^{ig\Phi(x)} \cdot \Psi(x), \tag{1.2}$$

where the phase shift $\Phi(x)$ is now dependent on the position x, the usual derivative has to be replaced (minimal coupling):

$$\partial_\mu \rightarrow \partial_\mu - igA_\mu. \tag{1.3}$$

Conserved Quantity	Strong Interaction	Electromagnetic Interaction	Weak Interaction
Energy	yes	yes	yes
Impulse	yes	yes	yes
Angular Momentum	yes	yes	yes
Charge	yes	yes	yes
Baryon Number	yes	yes	yes
Lepton Number	yes	yes	yes
Strangeness	yes	yes	no
Isospin	yes	no	no
C	yes	yes	no
P	yes	yes	no
T	yes	yes	no
CP	yes	yes	no
CPT	yes	yes	yes

Table 3: Main symmetry properties of the SM.

These are the theories which describe the interaction of fields $\Psi(x)$ via the gauge field A_μ, which means via the exchange of mediating bosons, which transfer momentum.
In addition to the continuous symmetries described above, also discrete symmetries play an important role in field theory. In field theories the most important discrete transformations are:

- C, Charge Conjugation: Particles are exchanged with anti-particles and vice-versa.
- P, Parity: The coordinate system is reversed, a vector $\vec{r}$ becomes $-\vec{r}$.
- T, Time Reversal: The direction of time is reversed.

The SM is further characterized by a high degree of symmetry. If the symmetries of the SM couplings were fully respected in nature, an electron would not be distinguished from a neutrino and the same would happen to protons and neutrons; their detectable differences are attributed to 'spontaneous' breaking of the symmetry (SSB). A summary of some of the most important conserved quantities is given in Table 3.

Lüders and Pauli [5, 6] have shown that any relativistic local field theory must be invariant under the combined operation CPT. However, this is not necessarily the case for a single operator C, P or T. While the electromagnetic and the strong interactions are invariant under all three transformations, the weak interaction violates P, as suggested by Lee and Yang [7] and shown by Wu and collaborators [8]. The weak interaction also violates C invariance. Christenson, Cronin, Fitch and Turlay [9] have shown that the combined transformation CP is also violated by the weak interaction. Given that the CPT theorem holds, CP violation implies that also T symmetry is broken.

2 Theory

2.1 The Kaon System

In the Standard Model particles are grouped together in multiplets of members with similar properties, these multiplets are characterized by the intrinsic spin and parity of its members. Kaons belong to the $J^P = 0^-$ meson octet illustrated in Figure 1.

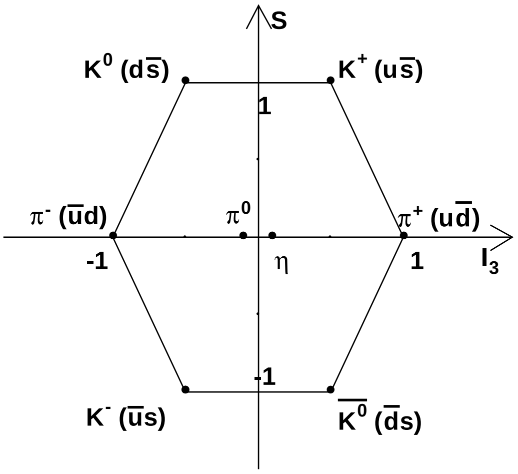

Figure 1: The octet of $J^P = 0^-$ mesons.

As it can be seen, the pairs (K^+,K^0) and ($\overline{K^0}$,K^-) form two isospin doublets with strangeness S = +1 and S = -1 respectively.

Neutral kaons, K^0 and $\overline{K^0}$, are particle and anti-particle, like K^+ and K^-, and are connected by the process of charge conjugation, which involves a reversal of the value of I_3 and a change of strangeness $\Delta S = 2$.

The combined operation of charge conjugation and parity operators over the neutral kaon system is:

$$\begin{aligned} CP(K^0) &= \overline{K^0}, \\ CP(\overline{K^0}) &= K^0, \end{aligned} \tag{2.1}$$

where the global phase has been chosen to be one.

2.2 Production of Neutral Kaons

Kaons can be produced via strong interaction. The baryon number, electric charge and strangeness (flavour) must be conserved:

$$
\begin{array}{ccccccccccc}
p & + & p & \rightarrow & K^0 & + & \Lambda & + & p & + & \pi^+ \\
p & + & n & \rightarrow & K^+ & + & \overline{K^0} & + & 2p & + & 2\pi^- \\
p & + & p & \rightarrow & \Xi^0 & + & p & + & K^+ & + & K^0
\end{array}
$$

As can be seen from these reactions, in proton-Nucleon collisions (pN collisions) the energy threshold to produce a $\overline{K^0}$ is higher than the energy threshold to produce a K^0 because the last ones can be produced in association with a hyperon and a nucleon, whereas $\overline{K^0}$ are produced only in association with a kaon, hyperon or antihyperon in order to conserve strangeness and at least another baryon is needed in order to conserve baryon number.

As far as *production* is concerned, the neutral kaon eigenstates are K^0 and $\overline{K^0}$.

2.3 Decay of Neutral Kaons

Kaons are the lightest particles with strangeness S, therefore they are not able to decay neither via the strong nor the electromagnetic interaction, they must decay via the weak interaction.
As the weak interaction violates strangeness conservation, the neutral kaon states K^0-$\overline{K^0}$ do not have a definite mass and lifetime and they may mix. However, one can form two independent linear superpositions of $|K^0\rangle$ and $|\overline{K^0}\rangle$, namely $|K_1\rangle$ and $|K_2\rangle$, with definite CP eigenvalues:

$$
\begin{aligned}
|K_1\rangle &= \frac{1}{\sqrt{2}}(|K^0\rangle + |\overline{K^0}\rangle) \qquad \text{CP} = +1, \\
|K_2\rangle &= \frac{1}{\sqrt{2}}(|K^0\rangle - |\overline{K^0}\rangle) \qquad \text{CP} = -1.
\end{aligned}
\tag{2.2}
$$

If CP symmetry holds, the K_1 and K_2 particles would be distinguished by their mode of *decay*. If the 2π- and 3π-decay modes are considered, the 2π state has CP = +1, whereas the 3π state can have CP = ±1, with CP = -1 heavily favored kinematically. The two- and three-pion decay modes have different phase-space factors and decay rates, the two-pion mode being much faster. If CP was conserved in weak interactions the decay $K_2 \rightarrow \pi^+\pi^-$ would be strictly forbidden.

However, in 1964 an experiment by Christenson, Cronin, Fitch and Turlay, first demonstrated that the long-lived state, K_2, can also decay to 2π with a branching ratio of order 10^{-3} [9].

The physical eigenstates with defined mass and lifetime differ from the CP eigenstates:

$$\begin{aligned} |K_\mathrm{S}\rangle &= \frac{1}{\sqrt{1+|\varepsilon|^2}}\left(|K_1\rangle + \varepsilon\,|K_2\rangle\right) \qquad \tau_S = (0.8940 \pm 0.0009) \times 10^{-10}\mathrm{s}, \\ |K_\mathrm{L}\rangle &= \frac{1}{\sqrt{1+|\varepsilon|^2}}\left(|K_2\rangle + \varepsilon\,|K_1\rangle\right) \qquad \tau_L = (5.17 \pm 0.04) \times 10^{-8}\mathrm{s}, \end{aligned} \tag{2.3}$$

where the subscript S means short-lived neutral kaon and the L means long-lived neutral kaon.
These states can be expressed in the $|K^0\rangle$ - $|\overline{K^0}\rangle$ basis as:

$$\begin{aligned} |K_\mathrm{S}\rangle &= \frac{1}{N_K}[(1+\varepsilon)|K^0\rangle + (1-\varepsilon)|\overline{K^0}\rangle], \\ |K_\mathrm{L}\rangle &= \frac{1}{N_K}[(1+\varepsilon)|K^0\rangle - (1-\varepsilon)|\overline{K^0}\rangle], \end{aligned} \tag{2.4}$$

with $N_K = \sqrt{2(1+|\varepsilon|^2)}$.

The K_L- and K_S-mesons have definite lifetimes, but they do not have definite strangeness or isospin. They are not charge conjugate states and have quite different decay modes (see Table 4) and lifetimes. A $K_L - K_S$ mass difference is therefore to be expected due to their different weak couplings.

The contribution of $\varepsilon\,|K_2\rangle$ to $|K_\mathrm{S}\rangle$ and $\varepsilon\,|K_1\rangle$ to $|K_\mathrm{L}\rangle$ is called *indirect CP violation* and has an absolute value of

$$|\varepsilon| = (2.271 \pm 0.017) \times 10^{-3} \text{ [3].} \tag{2.5}$$

The decay of a K_2 or K_1 into a final state of opposite CP via a weak $\Delta\mathrm{S} = 1$ transition is called *direct CP violation* in the decay. The parameter ε' measures the amount of CP violation in $\Delta\mathrm{S} = 1$ transitions (that is directly in the decay amplitude of the kaon). The measurement of the double ratio R gives access to the relative magnitude of direct CP violation,

K_L DecayModes	Γ_j/Γ	K_S DecayModes	Γ_j/Γ
$\pi^{\pm}e^{\mp}\nu_e$	$(38.78 \pm 0.28)\%$	$\pi^+\pi^-$	$(68.61 \pm 0.28)\%$
$\pi^{\pm}\mu^{\mp}\nu_{\mu}$	$(27.18 \pm 0.25)\%$	$\pi^0\pi^0$	$(31.39 \pm 0.28)\%$
$3\pi^0$	$(21.13 \pm 0.27)\%$	$\pi^+\pi^-\gamma$	$(1.78 \pm 0.05) \times 10^{-3}$
$\pi^+\pi^-\pi^0$	$(12.55 \pm 0.20)\%$	$\pi^{\pm}e^{\mp}\nu_e$	$(7.2 \pm 1.4) \times 10^{-4}$

Table 4: Decay rates of the weak eigenstates K_L and K_S. Short-lived kaons decay mainly in 2π, whereas long-lived kaons decay in semileptonic modes and 3π [3].

$$R = \frac{\Gamma(K_L \to \pi^0\pi^0)/\Gamma(K_S \to \pi^0\pi^0)}{\Gamma(K_L \to \pi^+\pi^-)/\Gamma(K_S \to \pi^+\pi^-)} \approx 1 - 6 \cdot \mathrm{Re}\left(\frac{\varepsilon'}{\varepsilon}\right). \tag{2.6}$$

The most accurate value for $\mathrm{Re}\left(\frac{\varepsilon'}{\varepsilon}\right)$ measured up to now is:

$$\mathrm{Re}\left(\frac{\varepsilon'}{\varepsilon}\right) = (14.7 \pm 2.2) \times 10^{-4} \text{ [11]}. \tag{2.7}$$

2.4 Strangeness oscillations

As it was shown in Section 2.2, neutral kaons can be produced in strong interaction processes. If the produced kaon is allowed to travel and decay through free space and strangeness is measured, components with both S = 1 and S = -1 whose intensities oscillate with time can be found. These oscillations are called *strangeness oscillations*, and they enable the mass difference between K_L and K_S particles to be measured with extraordinary accuracy.

The equation of motion for a linear combination of $|K^0\rangle$ and $|\overline{K^0}\rangle$ states, $|\Psi(t)\rangle = A(t)|K^0\rangle + B(t)|\overline{K^0}\rangle$, is:

$$i\frac{\mathrm{d}|\Psi(t)\rangle}{\mathrm{d}t} = (H_{strong} + H_{em} + H_{weak})|\Psi(t)\rangle = H|\Psi(t)\rangle. \tag{2.8}$$

Assuming the CPT theorem and hermiticity [12]

$$H = \begin{pmatrix} m - \frac{1}{2}i\Gamma & m_{12} - \frac{1}{2}i\Gamma_{12} \\ m_{12}^* - \frac{1}{2}i\Gamma_{12}^* & m - \frac{1}{2}i\Gamma \end{pmatrix},$$

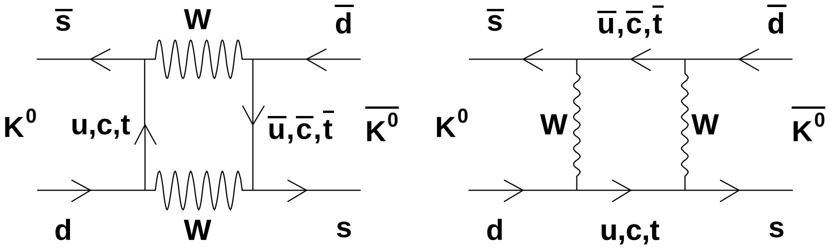

Figure 2: Box diagrams illustrating the ΔS = 2 mixing between $K^0$and $\overline{K^0}$.

with m and Γ being the mass and decay width of the $|K^0\rangle$ and $|\overline{K^0}\rangle$ states. m_{12} is responsible for virtual K^0-$\overline{K^0}$ mixing (i.e. oscillations between K^0 and $\overline{K^0}$) and Γ_{12} is responsible for real K^0-$\overline{K^0}$ mixing (i.e. due to decays to common decay channels of both K^0 and $\overline{K^0}$). In Figure 2 the box diagrams illustrating the mixing of neutral kaons are shown.

Since the states $|K_{\rm S}\rangle$ and $|K_{\rm L}\rangle$ are the eigenstates of the equation of motion, the wave functions of K_S and K_L at any time t in the rest frame of the particles are:

$$|K_S(t)\rangle = |K_S\rangle e^{-(\Gamma_S/2+im_S)t}, \tag{2.9}$$

$$|K_L(t)\rangle = |K_L\rangle e^{-(\Gamma_L/2+im_L)t}, \tag{2.10}$$

with $m_{S,L}$ and $\Gamma_{S,L}$ the masses and decay widths of the $K_{S,L}$-mesons. Starting with a pure K^0 beam at $t = 0$, i.e. B(0) = 0,

$$|\Psi(0)\rangle = |K^0\rangle = \frac{N_K}{2(1+\varepsilon)}[|K_S\rangle + |K_L\rangle],$$

and therefore at proper time t:

$$|\Psi(t)\rangle = \frac{N_K}{(1+\varepsilon)}[|K_S\rangle e^{-(\Gamma_S/2+im_S)t} + |K_L\rangle e^{-(\Gamma_L/2+im_L)t}]. \tag{2.11}$$

Rewriting the last expression using equations (2.4) and considering only up to the first order in ε

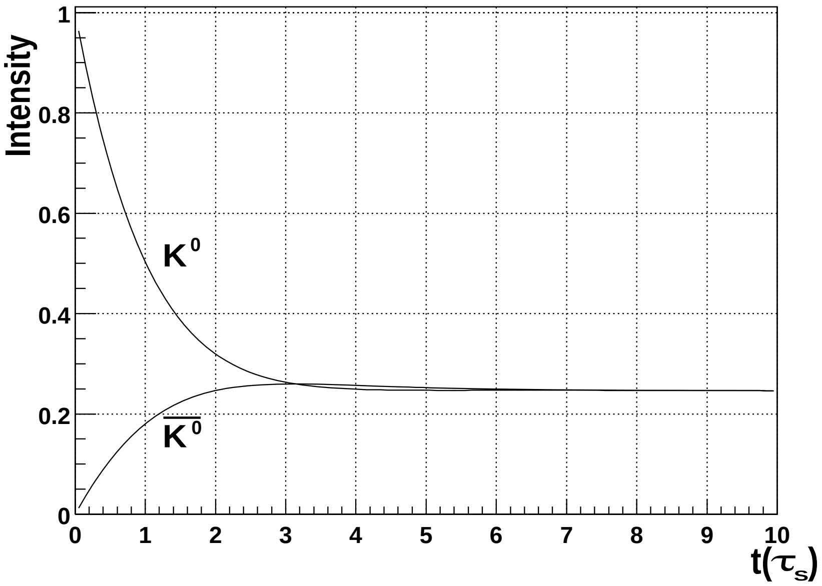

Figure 3: Oscillations of K^0 and $\overline{K^0}$ for an initially pure K^0 beam. An oscillation frequency of $\Delta m = 0.5\ \hbar\tau_S^{-1}$ is used in this representation.

$$|\Psi(t)\rangle \approx |K^0\rangle(e^{-(\Gamma_S/2+im_S)t} + e^{-(\Gamma_L/2+im_L)t}) + |\overline{K^0}\rangle(e^{-(\Gamma_S/2+im_S)t} - e^{-(\Gamma_L/2+im_L)t}), \tag{2.12}$$

which is no longer a pure K^0 beam.

The K^0 and $\overline{K^0}$ intensities at any time t are proportional to:

$$I(K^0) = |\langle K^0|\Psi(t)\rangle|^2 \propto [e^{-\Gamma_S t} + e^{-\Gamma_L t} + 2e^{-(\Gamma_S+\Gamma_L)t/2} cos(\Delta m \cdot t)], \tag{2.13}$$

$$I(\overline{K^0}) = |\langle \overline{K^0}|\Psi(t)\rangle|^2 \propto [e^{-\Gamma_S t} + e^{-\Gamma_L t} - 2e^{-(\Gamma_S+\Gamma_L)t/2} cos(\Delta m \cdot t)], \tag{2.14}$$

where $\Delta m = m_{K_L} - m_{K_S}$ is the mass difference between the K_L- and K_S-mesons. Thus, the K^0 and $\overline{K^0}$ intensities oscillate with the frequency Δm, i.e. the relative phase of K_S and K_L states of a given momentum is not constant in time. Figure 3 shows the variation to be expected for $\Delta m = 0.5\ \hbar\tau_S^{-1}$.

Starting with a pure K^0 beam and measuring the number of $\overline{K^0}$ as a function of the distance from the K^0 source, Δm can be deduced. To do that, one possibility is to count the number of K^0 and $\overline{K^0}$ semileptonic decays at different distances from the K^0 source and assume the $\Delta Q = \Delta S$ rule, which claims that the only semileptonic decays which are allowed for neutral kaons are $\overline{K^0} \rightarrow \pi^+ l^- \overline{\nu_l}$ and $K^0 \rightarrow \pi^- l^+ \nu_l$, whereas $\overline{K^0} \rightarrow \pi^- l^+ \nu_l$ and $K^0 \rightarrow \pi^+ l^- \overline{\nu_l}$ are forbidden by this rule (see Section 2.5.1).

The present world average value for Δm is:

$$\Delta m = (0.5300 \pm 0.0012) \times 10^{10} \hbar \mathrm{s}^{-1} \text{ [3]}. \tag{2.15}$$

A calculation of the mass difference, based on the quark exchanges in the box diagrams of Figure 2 neglecting the effects of any CP or CPT violation [13], gives the result

$$\Delta m = \frac{G^2}{4\pi^2} f_K^2 m_K m_c^2 cos^2\theta_C sin^2\theta_C, \tag{2.16}$$

where G is the coupling constant of the weak interaction, $f_K \approx 1.2\ m_K$ is the kaon decay constant, m_K is the mass of the kaon, m_c is the mass of the c-quark and θ_C is the Cabibbo angle, which is a constant that determines the weak coupling between different quark families [14].

2.5 Semileptonic Decays of Neutral Kaons

$K \rightarrow \pi^\pm l^\mp \nu_l$ decays are often referred to as K_{l3}. In the following K_{l3} will only denote neutral kaons semileptonic decays.

The amplitudes of K_{l3}-decays are not independent of one another but are related by CPT invariance, (approximate) CP invariance, the $\Delta S = \Delta Q$ rule, and the $|\Delta I| = \frac{1}{2}$ rule. Further restrictions on the amplitudes are also imposed by Cabibbo's hypothesis which assumes that the weak coupling between $W^\pm$ and quarks is modified by a linear combination of the quarks.

These decays are the combination of three interactions; weak, electromagnetic and strong. At low energies the quark structure is hardly seen and it is the hadrons themselves that show up. Non-perturbative strong interactions effects at low energy weak interactions force one to use phenomenological form factors in order to account for strong interaction effects in the matrix elements. The quarks only play a qualitative role in these decays, justifying selection rules and giving hints for the assignment of internal symmetry properties of the hadronic weak currents. Thus it is justified to use an effective V-A theory (see next section) if electromagnetic corrections are not considered. The lepton pair allows to determine the form factors that appear in the hadronic matrix element [15].

2.5.1 K_{e3} Matrix Elements

One of the basis of the V-A theory is the idea that the weak interaction can be explained as a product of currents [16]. The phenomenological Lagrange function for semileptonic decays can then be written like [12, 17]

$$\mathcal{L}_{\Delta S\neq 0} = S_\lambda^* j_\lambda + S_\lambda j_\lambda^*, \tag{2.17}$$

where S_λ is the hadron current and j_λ the lepton current

$$j_\lambda = i \sum_{e,\mu} u_l^+ \gamma_4 \gamma_\lambda (1+\gamma_5) u_{\nu_l}.$$

The formulation of the lepton current reflects the fact that it is only possible to have the coupling between a left-handed neutrino (right-handed antineutrino) and the corresponding antilepton (lepton).
The hadron current S_λ can be decomposed into a vector part S_λ^V and an axial part S_λ^A which takes into account parity violation in the weak interaction:

$$S_\lambda = S_\lambda^V + S_\lambda^A. \tag{2.18}$$

With the convention that the relative parity of K- and π- mesons is $+1$, in semileptonic decays the matrix element of S_λ^A does not play any role.

The most general matrix element for K_{l3} decays in the V-A theory can therefore be written as:

$$M = \frac{G}{\sqrt{2}}\, sin\Theta_C \ \left[f_+(q^2)(p_K+p_\pi)^\mu + f_-(q^2)(p_K-p_\pi)^\mu\right] u_l^+ \gamma_\mu (1+\gamma_5) u_\nu, \tag{2.19}$$

where Θ_C is the Cabibbo angle, f_+ and f_- are the vector form factors and p_K and p_π are the momenta of the kaon and pion, respectively.

Local creation of the lepton pair requires that the form factors to be functions only of the four-momentum transfer to the leptons, q^2 :

$$q^2 = (p_K - p_\pi)^2 = m_K^2 + m_\pi^2 - 2p_K \cdot p_\pi. \tag{2.20}$$

All the information on the strangeness changing weak current is contained in the q dependence of the form factors.

The use of the Dirac equation in the matrix element gives a factor m in front of the f_- form factor. The contribution to the transition rate in the case of electron and positron emission is therefore negligible due to the smallness of this mass compared to the kaon mass ($m_K \approx 1000 \cdot m_e$).

Following these approximations, for K_{e3}-decays only four form factors contribute to the matrix element:

$$\begin{aligned}
\langle \pi^- | S(x) | K^0 \rangle &= \frac{1}{2\sqrt{E_K E_\pi}} \big[(p_K + p_\pi) f \big] e^{iqx}, \\
\langle \pi^- | S(x) | \overline{K^0} \rangle &= \frac{1}{2\sqrt{E_K E_\pi}} \big[(p_K + p_\pi) g \big] e^{iqx}, \\
\langle \pi^+ | S^*(x) | \overline{K^0} \rangle &= \frac{1}{2\sqrt{E_K E_\pi}} \big[(p_K + p_\pi) \overline{f} \big] e^{iqx}, \\
\langle \pi^+ | S^*(x) | K^0 \rangle &= \frac{1}{2\sqrt{E_K E_\pi}} \big[(p_K + p_\pi) \overline{g} \big] e^{iqx}.
\end{aligned} \tag{2.21}$$

The various symmetry requirements impose different conditions on the form factors.

- **CPT Invariance**

  The net effect of a CPT transformation when a decay is represented by $\langle b|\mathcal{L}|a\rangle$ with $\mathcal{L}$ the Lagrange function is:

  $$\langle b|\mathcal{L}|a\rangle \rightarrow \langle \overline{a'}|\mathcal{L}|\overline{b'}\rangle = \langle \overline{b'}|\mathcal{L}|\overline{a'}\rangle^* \tag{2.22}$$

  where the bar means anti-particle and the prime signifies that spins are reversed.
  In K_{e3}-decays this means $\overline{f} = -f^*$ and $\overline{g} = -g^*$.

- **T Invariance**

  If T invariance holds, then all the form factors can be chosen to be real.

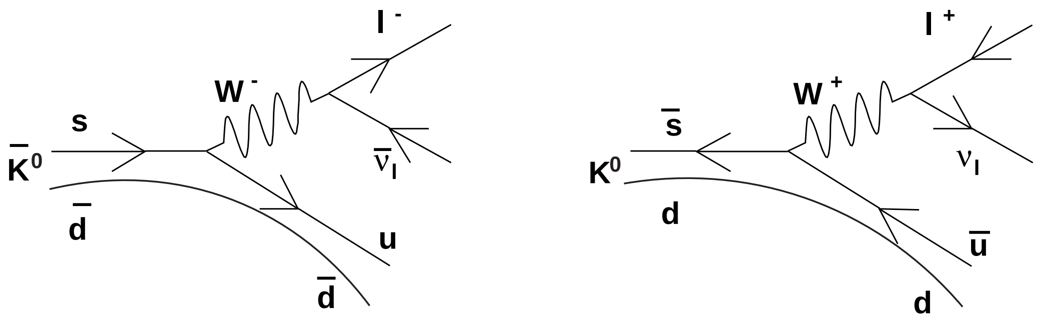

Figure 4: K^0 and $\overline{K^0}$ semileptonic decays. The $\Delta S = \Delta Q$ rule forbids $\overline{K^0} \to \pi^- \; l^+\nu_l$ and $K^0 \to \pi^+ \; l^-\nu_l$ decays.

- **CP Invariance**

  In case the transitions are invariant under CP:

$$f = -\overline{f} \; e^{i\alpha},$$
$$g = -\overline{g} \; e^{i\alpha}, \tag{2.23}$$

  where α is a constant phase depending on the relative phase between K^0 and $\overline{K^0}$.

- **The $\Delta S = \Delta Q$ Rule**

  The $\Delta S = \Delta Q$ rule implies that the change in the electric charge of the quarks involved in the weak coupling has to be equal to their change in strangeness. This rule forbids the decays $\overline{K^0} \to \pi^- l^+ \nu_l$ and $K^0 \to \pi^+ l^- \overline{\nu_l}$, i.e. $g = \overline{g} = 0$, being $K^0 \to \pi^- l^+ \nu_l$ and $\overline{K^0} \to \pi^+ l^- \overline{\nu_l}$ allowed (see Figure 4).The degree of violation of this rule is measured by the parameter $x = \frac{g}{f}$. The most accurate value for this parameter is:

$$\mathrm{Re}(x) = -0.0018 \pm 0.0041 \pm 0.0045 \; [18], \tag{2.24}$$
$$\mathrm{Im}(x) = 0.0012 \pm 0.0019 \; [18]. \tag{2.25}$$

- **The $|\Delta I| = \frac{1}{2}$ Rule**

  This rule establishes further connections between the amplitudes of neutral and charged kaons semileptonic decays. It states that the operators S^V_λ and $S^{V\dagger}_\lambda$ transform like components of an isospinor. The hadronic amplitudes for the different semileptonic decays can be rewritten as Clebsch-Gordan coefficients multiplied by a common numerical factor, the reduced matrix element M_0. If $|\Delta I| = \frac{1}{2}$:

$$\sqrt{2} \cdot M(K^+ \to \pi^0 l^+ \nu_l) = M(K^0 \to \pi^- l^+ \nu_l) \tag{2.26}$$

As can be seen from the Gell-Mann-Nishijima formula, $Q = I_3 + \frac{1}{2}(S + B)$, the $\Delta S = \Delta Q$ rule automatically implies the $|\Delta I| = \frac{1}{2}$ rule.

2.5.2 CP Violation in K_{e3}-decays

CP violation can also be observed in K_{l3}-decays. The probability to observe these decays is much higher for K_L- mesons than for K_S-mesons (see Table 4), for this reason, CP violation in semileptonic decays has only been studied in K_L-decays.

Both K_{Le3} charge modes are related via a CP transformation:

$$K_L \to \pi^+ l^- \overline{\nu_l} \quad \underset{\longleftrightarrow}{CP} \quad K_L \to \pi^- l^+ \nu_l, \tag{2.27}$$

where l means lepton and it can be either an electron or a muon.
If CP invariance is violated a small charge asymmetry is expected. The asymmetry is defined as

$$\delta_L = \frac{N(K_L \to \pi^- l^+ \nu_l) - N(K_L \to \pi^+ l^- \overline{\nu_l})}{N(K_L \to \pi^- l^+ \nu_l) + N(K_L \to \pi^+ l^- \overline{\nu_l})}, \tag{2.28}$$

where $N(K_L \to \pi^\mp l^\pm \nu_l)$ are the rates for the semileptonic l^+ and l^- charge modes respectively.

The weighted world's average for $\delta(\mu)$ and $\delta(e)$ is

$$\delta_L = 0.327 \pm 0.012\ [3]. \tag{2.29}$$

2.5.3 Interference between decay amplitudes of K_{Le3} and K_{Se3}

An arbitrary coherent mixture of K_L and K_S will show interference when decaying semileptonically or into any other common decay channel.

Using equations (2.4) the decay amplitudes of neutral kaons to both semielectronic charge modes can be expressed like:

$$\begin{aligned}A(K^0,e^\pm) &= \frac{N_K}{2(1+\epsilon)}\big[\langle\pi^\mp e^\pm\nu_e|H|K_S\rangle e^{-(\frac{\Gamma_S}{2}+im_S)t}\\ &\qquad \pm\langle\pi^\mp e^\pm\nu_e|H|K_L\rangle e^{-(\frac{\Gamma_L}{2}+im_L)t}\big],\\ A(\overline{K^0},e^\mp) &= \frac{N_K}{2(1-\epsilon)}\big[\langle\pi^\pm e^\mp\nu_e|H|K_S\rangle e^{-(\frac{\Gamma_S}{2}+im_S)t}\\ &\qquad \pm\langle\pi^\pm e^\mp\nu_e|H|K_L\rangle e^{-(\frac{\Gamma_L}{2}+im_L)t}\big].\end{aligned} \tag{2.30}$$

In strong interactions quarks are always created in pairs, this means that for each quark the corresponding antiquark is always created. In high energetic proton-nucleon collisions for some examples), only the valence quarks from the nucleons contribute to the collision. If one considers the probabilities of creating $d\overline{d}$ and $s\overline{s}$ pairs, the K^0 production can be considered to be either the creation of both an $s\overline{s}$ and a $d\overline{d}$ pair or the creation of an $s\overline{s}$ pair and the use of one of the d valence quarks of the nucleon (proton: uud, neutron: udd). Hence the probability of production of K^0 is larger than the probability of $\overline{K^0}$ production for a given energy of the kaons [19]. This difference in the production of K^0 and $\overline{K^0}$ is often parameterized as $D(p) = \frac{N(K^0)-N(\overline{K^0})}{N(K^0)+N(\overline{K^0})}$ being this ratio referred to as 'Dilution Factor'. The Dilution Factor has been measured by the NA31 experiment at CERN [20] for the kaon energies shown in Figure 5.

If kaons are created incoherently, the number of decays in both charge decay modes is:

$$\begin{aligned}N^+ &= N(K^0)\cdot|A(K^0,e^+)|^2 + N(\overline{K^0})\cdot|A(\overline{K^0},e^+)|^2,\\ N^- &= N(K^0)\cdot|A(K^0,e^-)|^2 + N(\overline{K^0})\cdot|A(\overline{K^0},e^-)|^2,\end{aligned} \tag{2.31}$$

where N^+ is the rate of semileptonic decays producing positrons and N^- is the rate of semileptonic decays producing electrons.

Substituting equations (2.30) in the last expressions, assuming the validity of the $\Delta S = \Delta Q$ rule and the CPT theorem, and neglecting CP violation effects:

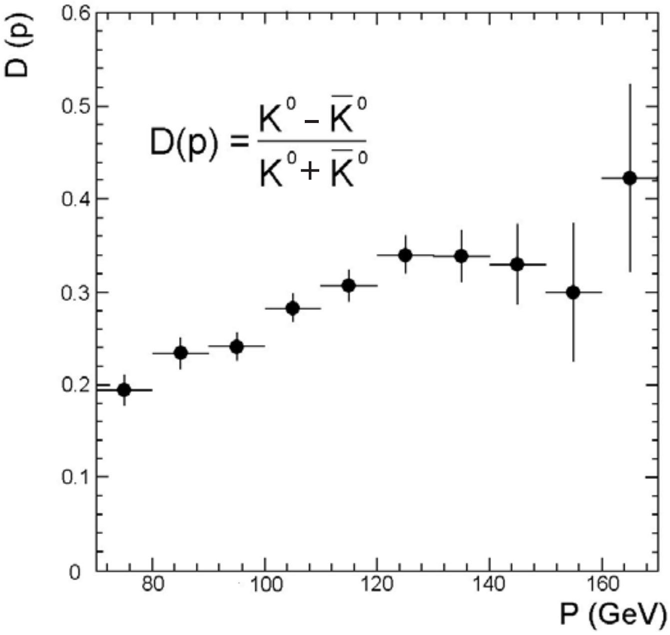

Figure 5: The Dilution Factor. The above figure shows the variation of the dilution factor as a function of the energy of the produced kaons. The measurement was performed by NA31 with an incoming proton beam of 450 GeV/c of momentum and a production angle of 3.6 mrad [20].

$$N^+ = S(p) \cdot \left[\eta^2 \cdot e^{-\Gamma_S t} + e^{-\Gamma_L t} + 2 \cdot e^{-(\Gamma_L + \Gamma_S)t/2} \cdot \eta \cdot D(p) \cdot cos(\Delta m \cdot t)\right],$$

$$N^- = S(p) \cdot \left[\eta^2 \cdot e^{-\Gamma_S t} + e^{-\Gamma_L t} - 2 \cdot e^{-(\Gamma_L + \Gamma_S)t/2} \cdot \eta \cdot D(p) \cdot cos(\Delta m \cdot t)\right], \tag{2.32}$$

with

$$\eta = \frac{\langle \pi^{\mp} e^{\pm} \nu_e | H | K_S \rangle}{\langle \pi^{\mp} e^{\pm} \nu_e | H | K_L \rangle},$$

$S(p)$ the production spectrum of $K^0 + \overline{K^0}$ as a function of the momentum of the kaons, and $D(p)$ the dilution factor.
In Figure 6 (left), equations (2.32) are shown in units of K_S-lifetimes. In Figure 6 (right), the difference between equations (2.32) and therefore

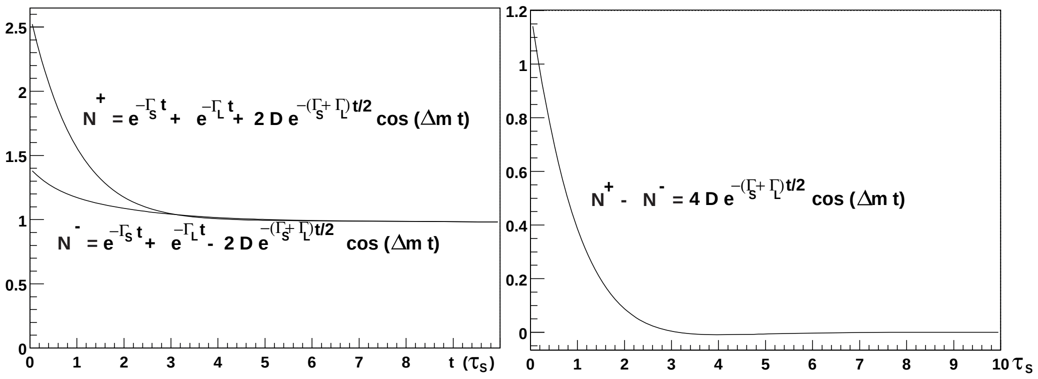

Figure 6: Interference between decay amplitudes of $K_{S,L}$ semileptonic decays decays. Left: time evolution of the intensity of $K_{S,L} \to \pi^{\pm}e^{\mp}\nu_e$ decays as shown in eqs (2.32). Right: time evolution of the interference term. The following values are used in the above representations: $S(p) = 1$, $\eta = 1$, $D = 0.3$, $\Delta m \cdot \tau_S = 0.5 \cdot \hbar$ and the tabulated values of $\tau_{S,L}$ [3].

the oscillation term is shown. The following values are used in the representations: $S(p) = 1$, $\eta = 1$, $D = 0.3$, $\Delta m \cdot \tau_S = 0.5 \cdot \hbar$ and the tabulated values of $\tau_{S,L}$ [3].

Assuming the validity of the $\Delta S = \Delta Q$ rule and CPT conservation:

$$\Gamma(K_S \to \pi^{\mp}e^{\pm}\nu_e) = \Gamma(K_L \to \pi^{\mp}e^{\pm}\nu_e), \tag{2.33}$$

and therefore $\eta = 1$.

In this analysis both the BR($K_S \to \pi^{\mp}e^{\pm}\nu_e$) and the mass difference $\Delta m = m_{K_L} - m_{K_S}$ are studied and measured from a fit of equations (2.32) to the selected $K_{S,Le3}$ data sample.

3 The NA48 experiment

The NA48 experiment is a collaboration between institutes and universities from Cagliari, Cambridge, CERN, Dubna, Edinburgh, Ferrara, Firenze, Mainz, Orsay, Perugia, Pisa, Saclay, Siegen, Torino, Warschau and Wien. It is the 48th experiment in the North Area of the SPS (Super Proton Synchrotron) at CERN (European Center for Nuclear Research), Geneva.

This experiment started its data taking in 1997. The main purpose of it was the measurement of the parameter of direct CP violation $\frac{\varepsilon'}{\varepsilon}$ with a precision of 2×10^{-4}, which means an improvement by a factor three of previous results [21]. The experiment was designed with two nearly collinear K_S and K_L beams produced concurrently [22]. In this way, all four decay modes $K_{L,S} \rightarrow \pi^0\pi^0$ and $K_{L,S} \rightarrow \pi^+\pi^-$ were measured simultaneously and systematic effects in the measurement of $\frac{\varepsilon'}{\varepsilon}$ were minimized.

The beam configuration was modified in special run periods in order to measure rare decays of the K_S-meson and hyperon decays. During these periods there was only one beam which was produced at the K_S target, the K_S beam. The data used in this analysis were collected in one of these special runs of about two days long in September of 1999, the also called '1999 K_S High Intensity Run'. In the next sections the configuration of the experiment during these runs is explained.

3.1 The Beam

The layout of the beam geometry is shown in Figure 7. The beam is derived from the CERN SPS proton beam, which has an energy of 450 GeV. A proton spill of 2.5 s duration is extracted every 14.4 s to the NA48 experimental area. The nominal intensity is 1.1×10^{12} protons per burst.

After three stages of collimators the proton beam is directed onto the named K_S target, which consists of four 10 cm long Beryllium rods with a diameter of 2 mm. This target is in vacuum and is located at 7.2 cm above the horizontal axis of the detector, the production angle is 4.2 mrad. The target and the following collimator apertures are precisely aligned along an axis pointing downwards at 0.6 mrad, which intersects the horizontal axis and passes through the center of the detectors at a longitudinal distance of 120 m from the target. Downstream of the target, the beam enters the field of a strong, vertical sweeping magnet, the gap of which is filled with tungsten-alloy inserts containing a passage for the neutral beam. This passage is

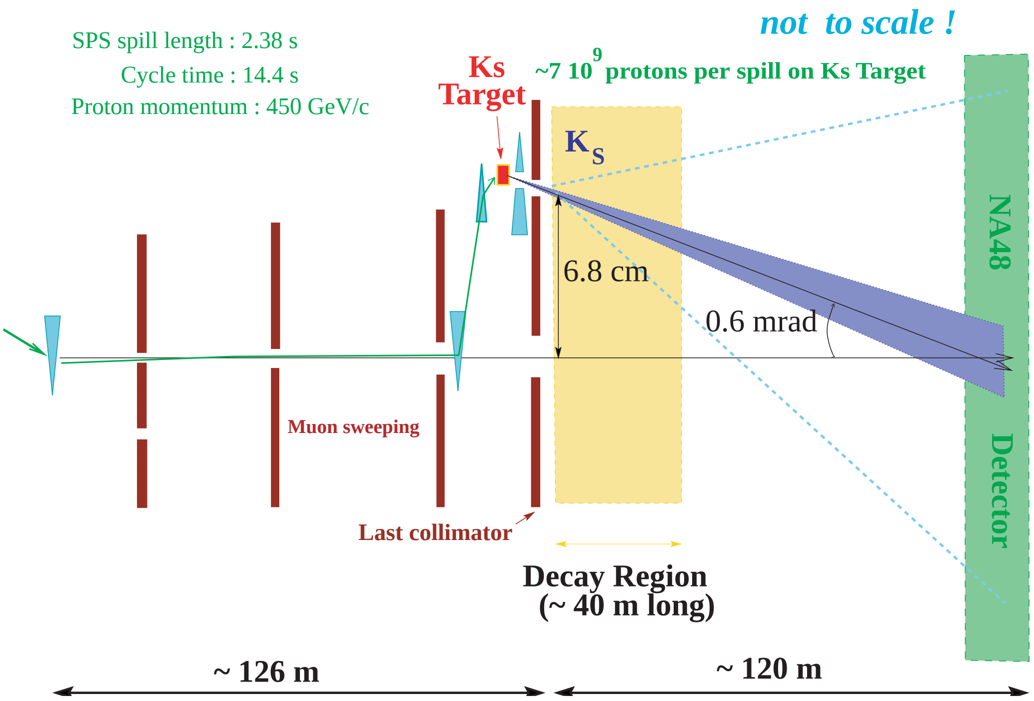

Figure 7: Schematic Layout of the Beam Geometry of the '1999 K_S High Intensity Run'.

shaped to absorb the remaining primary protons at a point where they are separated from the neural beam, and to intercept the curved trajectories of all charged secondary particles from the target. The magnet is followed by a steel collimator, which is fitted with further precisely-bored inserts, ranging from a beam defining aperture of 3.6 mm at 4.8 m from the target to a final diameter of 6.0 mm at the exit, 6.0 m after the target, where the K_S beam enters the decay volume. The K_S collimator defines the direction and divergence of the beam ($\sim \pm 0.375$ mrad). The overall length of the K_S collimator is close to the optimum $1c\tau_S$, where the ratio of useful K_S flux to neutron- and photon-induced background from the defining aperture is maximum. Due to the much longer lifetime of the K_L-mesons, the produced K_L component decays at a constant rate in the decay volume. For a mean energy of the produced kaons of 110 GeV, about 7.5 K_S lifetimes can happen within the decay region, which means that 99% of the K_S decays will happen there. For this reason this beam is called the 'K_S beam'.

3.1.1 The Beam Subdetectors

There are two subdetectors associated with the beam, the K_S monitor and the beam intensity monitor.

The K_S monitor is located in the iron support structure of the K_S target. Four scintillator counters give a signal proportional to the instantaneous intensity of the proton beam impinging on the target. Four veto counters, surrounding the beam pipe upstream of the K_S monitor, ensure that protons missing the target are not counted directly [23].

The beam intensity monitor is used to measure the beam profiles right after the beam dump. It is also used to generate a trigger for uncorrelated events. It is made of a matrix of scintillating fibers with an active area of 1.8×1.8 cm^2 read out by 16 photo-multipliers.

3.2 The Decay Volume

The decay volume is a cylindrical region of 89 m long and 10^{-4} mbar of pressure where the main part of the decays studied happen.
This volume is divided into two sections with different radius each one. The first section has a diameter of 1.92 m and 39 m of length. The second section has 2.4 m of diameter in order to contain the decay products with higher angles. This section finishes with a 0.9 mm thick concave Kevlar window (0.003 interaction lengths) followed by the helium tank which contains the magnet spectrometer. Within this tank, starting in the middle of the Kevlar window and until the end of the detector, the neutral beam derived from the target is transported through a beam pipe of 153 mm of diameter. In this way, background coming from the interactions of neutral particles is avoided. The layout of the main components of the detector can be seen in Figure 8.

3.3 The Magnet Spectrometer (DCH)

The magnet spectrometer is used to reconstruct tracks and momenta of charged particles.

The spectrometer consists of a dipole magnet and two drift chambers on each side of it (see Fig. 9). The whole spectrometer is situated inside a helium tank which keeps the probability of multiple scattering of charged particles small. The pressure inside the helium tank is 1 atm in order not to damage

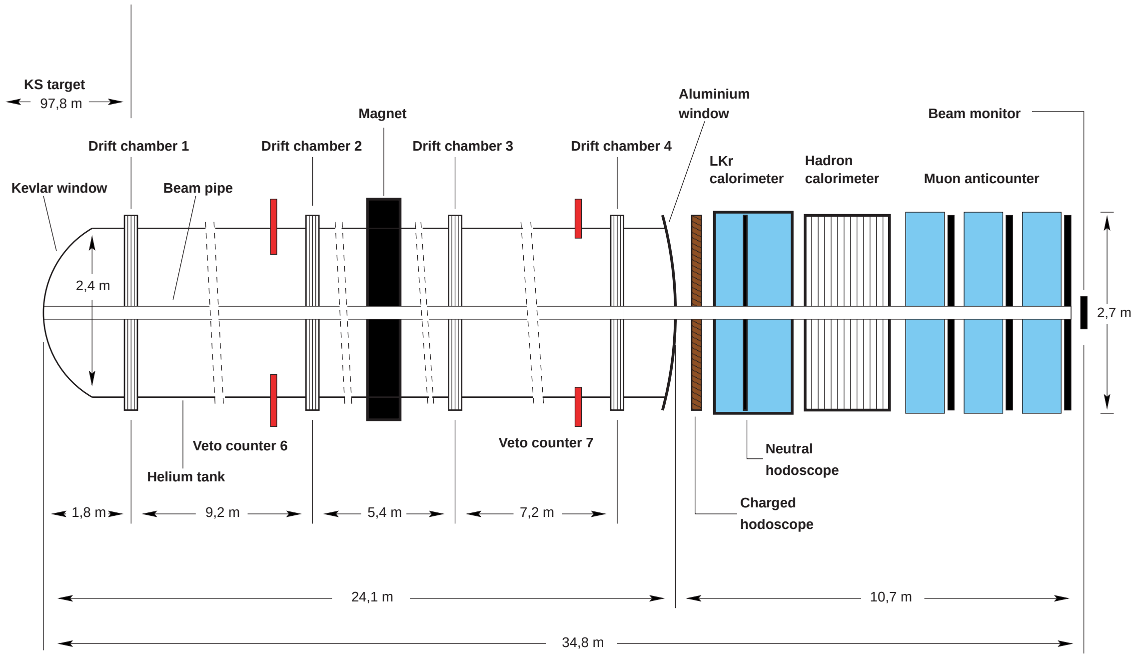

Figure 8: Layout of the main detector components of the NA48 detector.

the walls of the chambers.

The integral field of the magnet is 0.84 Tm at a nominal current of 1200 A. This is equivalent to a change in the x-direction of the momentum of 265 MeV/c. The four drift chambers consist of eight planes of 256 wires each one. The spacing of the sense wires is 1 cm. The eight planes are oriented in four different directions orthogonal to the beam axis: 0° (x,x'), 90° (y,y'), −45° (u,u'), 45° (v,v'). Each view contains two staggered planes of wires to resolve left and right ambiguities. The first, the second and the forth drift chamber are connected completely to the read-out. In chamber number three only the x- and y-views are read. This is possible because even without drift chamber number three, the vertex can be calculated from the information from drift chambers one and two. The momentum can then be calculated with the knowledge of the field map and the track segments reconstructed in chamber four (see Section 4.2).

The spatial resolution of one view is $\sim 90\mu m$, this leads to a momentum resolution of

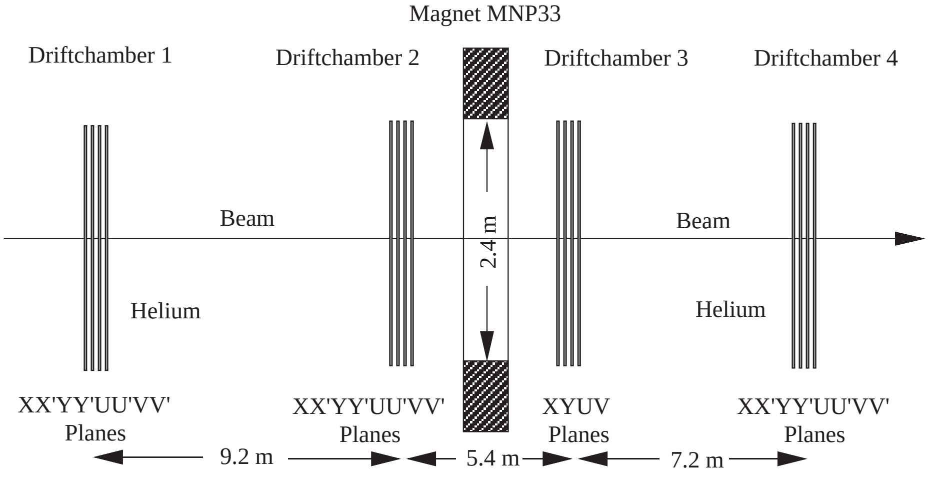

Figure 9: The Magnet Spectrometer.

$$\sigma_p/p \simeq \sqrt{(0.48\%)^2 + (0.009\% \times p[GeV])^2} \qquad (3.1)$$

The information of this detector can be used to compute the vertex and the momentum of the charged decay products.

3.4 The Hodoscope for Charged Particles

The hodoscope is used to measure the event time of charged events and to generate a fast trigger signal for decays into charged particles.

The hodoscope is built of vertical and horizontal planes which are located between $z = 119.5$ m and $z = 120.3$ m. Each plane is divided into four quadrants with 16 plastic scintillators each of which are read by photomultipliers (see Fig. 10). The thickness of the scintillators is 2 cm and the width varies from 6.5 cm in the region close to the beam pipe to 9.9 cm in the outer part.
The hodoscope can also be used as a fast trigger signal for charged events because it allows us to get information about the number and topology of the charged decay products according to the quadrants which are hit by the tracks. For instance, the Q_x condition would define two hits in opposite quadrants which is very useful in two body decays of charged tracks because there the transverse momentum must be zero.

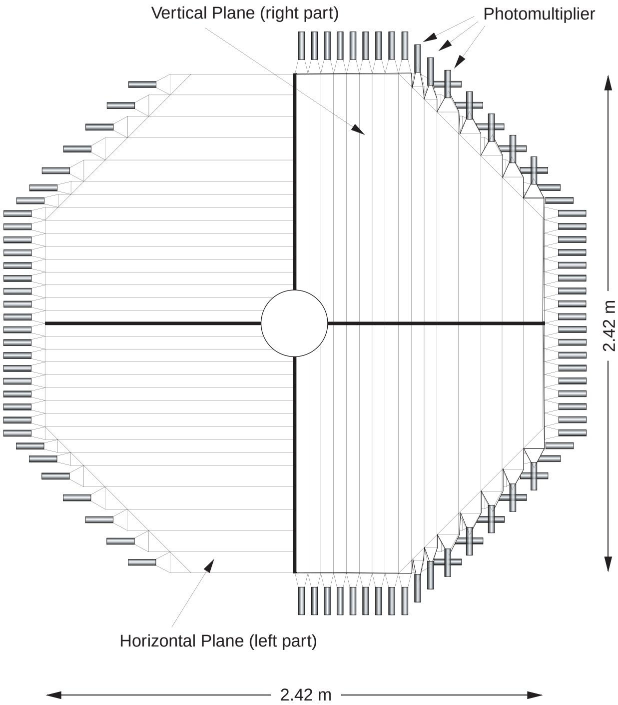

Figure 10: The Hodoscope for Charged Particles.

3.5 The LKr Electromagnetic Calorimeter

A large, quasi-homogeneous liquid krypton electromagnetic calorimeter (LKr) is used to measure the energy and position of those decay products which interact electromagnetically. This calorimeter was designed for very high particle rates and excellent energy, space and time resolution.

The active volume of the calorimeter is 9 m^3 of liquid krypton at 121 K. The radiation length for the liquid krypton is $X_0 = 4.7$ cm. The calorimeter has an inner radius of 1.28 m and is 1.25 m long, which corresponds to 27 X_0. This permits to measure almost completely the energy deposited by electromagnetic showers with a very good energy resolution.

The LKr calorimeter consists of 13248 cells with a cross section of 2 cm × 2 cm. This cells structure improves the spatial resolution and allows to distinguish photons which are very close. Each cell consists of three Cu-Be ribbons, two cathodes and one anode, which are guided by five spacer plates and two more (see Fig. 12), the back and the front plates, and are set in zig-zag with an angle of 48 mrad. This allows us to reduce non-uniformities

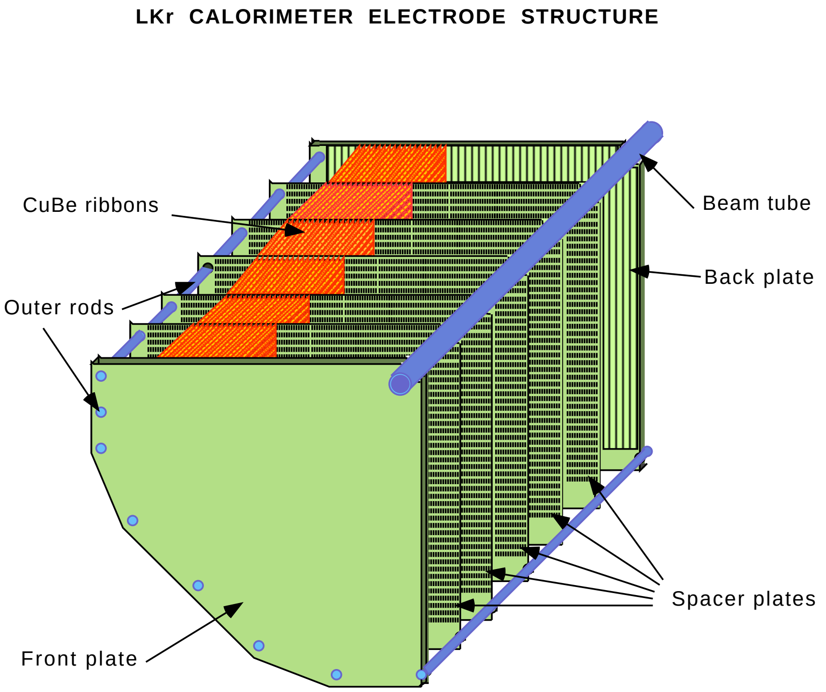

Figure 11: The Electromagnetic Calorimeter.

coming from the relative position of the shower within the cell.

During the 1999 data taking, the following resolutions where achieved [21]:

- Energy Resolution $\frac{\sigma(E)}{E} = \sqrt{(\frac{3.2\%}{\sqrt{E/\mathrm{GeV}}})^2 + (\frac{0.125}{E/\mathrm{GeV}})^2 + (0.5\%)^2}$
- Space Resolution $\sigma(x) < \frac{5.4\ \mathrm{mm}}{\sqrt{E/\mathrm{GeV}}}$
- Time resolution $\sigma(t) < 300\ \mathrm{ps}\ \ (E = 50\ \mathrm{GeV})$

3.6 The Hodoscope for Neutral Particles

In addition to the time resolution of neutral events performed by the calorimeter, the neutral hodoscope (NHOD) provides another measurement of this time which is completely independent of the energy measurement.
The hodoscope for neutral decay modes is located at the second spacer plate inside the electromagnetic calorimeter. This detector consists of scintillating fibers contained inside 256 tubes of 7 mm diameter. The NHOD is placed at the position of the shower maximum ($\sim 9.5X_0$). A total of 10080 fibers

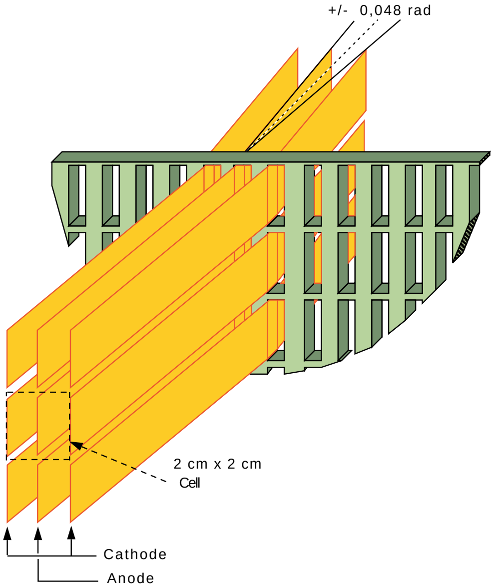

Figure 12: Cells structure of the electromagnetic calorimeter.

are arranged in 4 quadrants with eight read-out channels each. The read-out system is the same as for the charged hodoscope.

3.7 The Hadron Calorimeter

The hadron calorimeter (HAC) is used to measure the energy and position of hadrons. These particles only deposit a small part of their energy in the electromagnetic calorimeter. As the momentum and position are measured in the spectrometer with much higher precision, the HAC is mainly used in the trigger to form the total energy sum of a given event.

The hadron calorimeter is an iron sandwich calorimeter with two modules (front and back module). The HAC is 1.42 m deep, resulting in 6.7 nuclear interaction lengths. It consists of a total number of 48 2.5 cm thick steel plates and 49 scintillating planes, divided into 44 strips per plane (see Figure 13). The strips are alternatingly horizontally and vertically oriented. Strips are grouped together such that the read-out is projective: subsequent strips with the same orientation are read out by a single photo-multiplier.

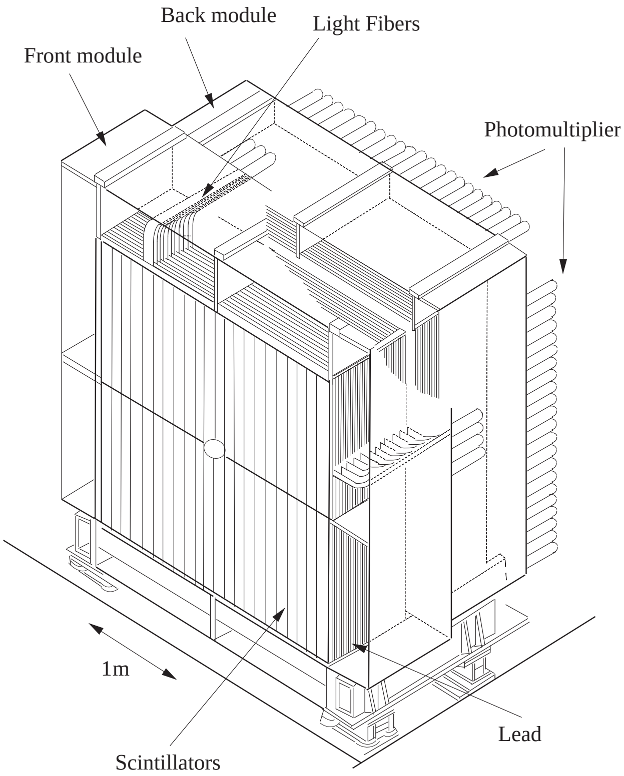

Figure 13: The Hadron Calorimeter.

3.8 The Muon Veto Counter

The primary task of the muon veto is to identify the $K_L \rightarrow \pi\mu\nu_\mu$ decays. It can also be used as a positive trigger component to study rare kaon decays. This detector consists of three planes of plastic scintillator. The first two planes, horizontally and vertically oriented, are 10 mm thick and form the actual detector whereas the third plane is 6 mm thick and is used for efficiency studies of the muon veto itself. Each plane is preceded by a 0.8 m thick iron wall to ensure that all other particles except for muons are stopped inside the iron.

3.9 The Trigger and the Data Acquisition System

Trigger and data acquisition are designed to cope with the high rates of the NA48 detector. The trigger consists of two stages which reduce the total output rate to about 5 kHz with a minimum dead time. The PC-Farm collects the data from the various subdetectors and builds complete events and bursts. The raw data are then processed by the Level 3 Trigger/Real Time Reconstruction program (L3/RTR). Several output streams are saved on tape. In Figure 14 a scheme of the data acquisition system is shown.

3.9.1 The Level 1 Pre-Trigger

The Level 1 Pre-Trigger is a fast two particles trigger. One common 960 MHz clock is used as time reference which is distributed to all sub-systems. The task of this trigger is to reduce the input rate for the next stage to about 70 kHz.

This trigger combines the information from the muon veto counters and calorimeters. This stage is controlled by the L1 Trigger Supervisor. The L1 Trigger Supervisor has to decide whether a trigger condition is fulfilled within 5 μs.

The Level 1 Pre-Trigger uses the following signals:

Q1 : at least one coincidence of one horizontal and one vertical channel in the hodoscope
Q2 : at least two coincidences of horizontal and vertical channels of the hodoscope
Q_x : coincidences in opposite quadrants of the hodoscope
E_{HAC} : energy of the hadron calorimeter
E_{tot} : total energy of both calorimeters
2track : two tracks in the drift chambers

The pre-selection of decays into charged particles uses as a pre-trigger the conditions from the charged hodoscope, the information about the energies from the calorimeters and the DCH information about the tracks. According to this information, the Level 1 Trigger Supervisor decides whether the event is accepted. In case it is accepted, the event is passed to the next trigger stage, the Level 2 Trigger Supervisor.

3.9.2 The Level 2 Trigger

The second trigger level uses the so called 'neutral Trigger' to look for decays into neutral particles whereas the 'Massbox' Trigger is used to look for decays into charged particles.

The neutral Trigger is integrated in the electromagnetic calorimeter. In this trigger, it is studied whether all the showers which have been registered

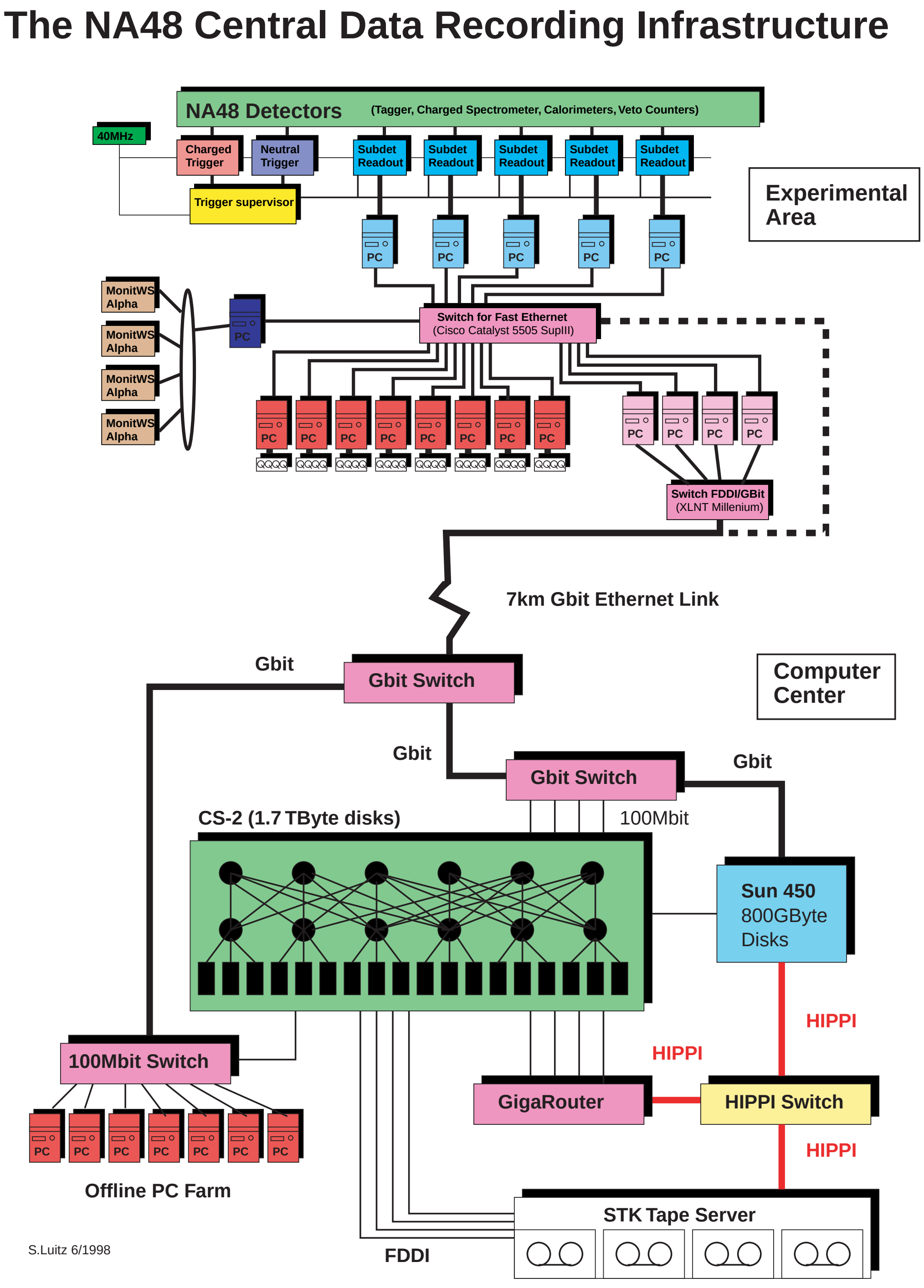

Figure 14: The Data Acquisition System.

at the calorimeter happened at the same time or there are some random showers.

In the case of charged decays, the Massbox Trigger calculates the invariant mass and the decay vertex of charged decays using the information from the magnet spectrometer.

It takes the Level 2 Trigger Supervisor 100 μs to decide about the event. If the answer is positive, the subdetectors are asked to record the information about this event.

3.9.3 The Online PC Farm

After a positive decision from the Level 2 Trigger Supervisor, the data from the event are read by the Online PC-Farm. This PC-Farm consists of eleven subdetector-PCs, which get the data from the subdetectors, and twelve Event-Building-PCs, which collect all the data belonging to one event and rebuild each burst and afterwards send the data-bursts to the CERN computing center.

3.9.4 The Level 3 Trigger

The raw data are processed by the Level 3 Trigger at the Offline PC-Farm of the CERN computing center and then they are saved on tape.
The Level 3 Trigger runs over fully reconstructed events, which means that it gets all the information available from the subdetectors which belong to one event. It is possible then to apply some selection criteria in order to pre-classify events so that the access to the desired data is faster.

The Level 3 Trigger has three tasks:

1. The selection of events which are used for calibration and for checks of data quality during the data taking.
2. The pre-selection of events during data re-processing which will be used for the final analysis.
3. The reduction of the data volume in order to increase accessibility by using the COmPACT output format (Compact Optimized Program to Access Countless Terabytes [26]). This compact format is used in the analysis of the data.

Several output streams are saved on tape.

3.10 The 1999 K_S High Intensity Run Data Taking

The '1999 K_S High Intensity Run' were 48 hours of data taking divided in two periods between August and September of 1999. The first running period was 8 hours long at the end of August of 1999. The second running period was at the beginning of September of the same year and lasted 40 hours.

In this special run, protons coming from the SPS were impinging directly on the K_S target, i.e. there was no K_L beam. This period was called the '1999 K_S High Intensity Run' because an intensity of about 5×10^9 protons per spill on the K_S target was achieved - 100-200 times more intensity at the K_S target than in normal running periods. There was a total flux of 3×10^8 kaon decays with a mean energy of about 110 GeV. The main features of this run together with the trigger conditions used in this analysis are summarized in Table 5.

The Hyperon-Trigger

For the Hyperon Level 1 Pre-Trigger it was required at least one coincidence between the two planes in the charged hodoscope in addition to a minimum total energy from the calorimeters of 35 GeV and at least two hits in the first drift chamber.

In the Level 2 Charged Trigger, the Massbox Trigger, it was required a relaxed closest distance of approach (cda) cut to determine the vertex (see Section 4.4.4). The relaxed cda cut (at 8 cm) allows to trigger on semileptonic Ξ^0-decays. In order to reject the dominant $K_S \to \pi^+\pi^-$ decays, a cut on the invariant mass of the two charged tracks (assumed to be pions) was applied around the K_S mass. To exploit the presence of a baryon in the final state, the ratio of the momenta of the two tracks was required to be greater than 4-5 or smaller than 1/4-5. Downscaling factors between 4 and 10 (one event out of four triggered events is accepted) had to be applied in order to reduce the high rate of the trigger. See Section 6.1 for more details about this trigger.

	Run 1 (August 1999)	Run 2 (September 1999)
Duration	8 hours	40 hours
Proton Intensity (ppp)	$\sim 2 \times 10^9$	$\sim 5 \times 10^9$
Production Angle (mrad)	-4.2	-4.2
Beam Divergence (mrad)	0.375	0.375
Current in the Magnet	1200 A	-1200 A
Total Number of Triggers	$\sim 23 \times 10^6$	$\sim 150 \times 10^6$
Level 1 Hyp. Pre-Trigger	$Q_x \times E_{tot} \times 2track$	$Q1 \times E_{tot} \times 2track$
Level 2 Hyp. Trigger downsc.	10	4-8

Table 5: Main features of the 1999 K_S High Intensity Run.

4 Reconstruction of Events

Most of the kinematic variables used in this analysis make use of the reconstruction of the information obtained from the drift chambers and the electromagnetic calorimeter.

The reconstructed information from the different subdetectors concerning the events (tracks, momentum, energy of the clusters, etc.) is available in COmPACT format and is provided by the Level 3 Trigger program (see Section 3.9.4).

In this section the reconstruction of the information obtained from the drift chambers and the electromagnetic calorimeter is described together with the main kinematic variables used in the analysis.

4.1 The System of Coordinates of the NA48 detector

The direction of the z-axis is defined by the longitudinal direction of the beam pipe and it points towards the end of the detector. The y-axis contains the K_S target and points upwards. These two axis are perpendicular to each other and do intersect at the origin of coordinates in the middle of the beam pipe. The orientation of the x-axis is such that the three axis form a righthanded system.

4.2 Reconstruction of the DCH Information

The reconstruction of the drift chambers information is split into two parts. In the first part tracks are built without using the drift time information. In the second part drift times are used to refine the tracks.

As a first step, hits in the A and B planes of each view are grouped together to clusters. Two clusters in different plane projections can define a space point. The planes can have two hits so that a cluster consists of 1, 2 or 3 hit wires. Track segments are formed from the clusters of identical views in chamber one and two. A segment is a projection of a track in one of the views. The angle of one segment with respect to the beam direction must be smaller than 20 mrad. The four segments of the views build one track. In order to reduce the number of tracks, the segments are divided into two groups according to their 'quality'. One track is accepted when at least three of the four segments are included in the 'best quality' group. In addition, the tracks cannot have any common space point. The successful tracks are then extrapolated to chamber four.

In chamber four space points are built from the clusters. If a space point is found in a certain search region around the extrapolated intersection point of a track with drift chamber number four, this point is associated to the track. The search region is equivalent to a requirement on the bending angle of the track.

In the second part, the drift time information is used to increase the accuracy of the track information. Ambiguities are resolved and mini-tracks are formed. The intersection points can now be exactly resolved and form mini-tracks. The mini-tracks are selected with a χ^2 test (the mini-tracks from the first two drift chambers are combined in drift chamber number four with the new space points, the 'real' tracks are then obtained by means of χ^2 tests). For each of the selected tracks the time information is stored.

The track momentum and the sign of the charge are determined using the measured space points and the integral of the magnetic field along the track. A map of the magnetic field was determined using a Hall probe. The z-position of the decay vertex for pairs of tracks with opposite charge is defined by the closest distance of approach (cda) of the two tracks. The x- and y-coordinates of the decay vertex are defined as the point in the middle of the two tracks.

The magnitude of the momentum of a charged particle can be evaluated by considering the deviation of the track due to the magnetic field with the following parameterization:

$$\begin{aligned} x &= x(0) + \frac{dx}{dz}(z - z(0)) + \frac{C_x}{p}, \\ y &= y(0) + \frac{dy}{dz}(z - z(0)) + \frac{C_y}{p}, \end{aligned} \tag{4.1}$$

where C_x and C_y are the integrated magnetic field components between z_0 and z in the x- and y-direction, p is the momentum, and x and y the space coordinates for a given z [27].

The space components of the momentum are:

$$\begin{aligned} p_x &= \frac{dx}{dz} \cdot p \cdot N, \\ p_y &= \frac{dy}{dz} \cdot p \cdot N, \\ p_z &= p \cdot N, \end{aligned} \tag{4.2}$$

where $\frac{dx}{dz}$ and $\frac{dy}{dz}$ are the slopes of the track in the x- and y-direction before passing through the magnet and N is the normal vector in the z-direction,

$$N = \frac{1}{\sqrt{(dx/dz)^2 + (dy/dz)^2 + 1}}. \tag{4.3}$$

4.3 Reconstruction of the LKr Electromagnetic Calorimeter Information

The first step of the LKr calorimeter reconstruction is to convert the ADC counts into energy for each cell. The pedestal introduced by a pulser situated after each pre-amplifier is subtracted. The conversion factor is obtained from the electronic calibration. Seed cells which are local maximums compared to the eight surrounding cells and have an energy greater than 0.2 GeV are searched. Only seeds which are a local maximum in time with the event time are kept. Clusters are built using the cells within 11 cm radius around the seed cell. For each of these cells the energy and time are determined using a digital filter. The energy of each cell is corrected by a factor found from the analysis of data depending on the run period (inter-cell calibration). The cluster energy is the sum of the energy of each cell belonging to the cluster. The cluster time is given by the time information of the seed cell, the surrounding cells are energy weighted in order to determine the event time.

The center of gravity of each cluster is calculated in order to determine the cluster position. The position is corrected using a functional dependency found in detailed Monte Carlo studies. The cluster energy is corrected in order to account for effects of different distances of the shower core from the anode. For overlapping clusters a correction taking into account the energy sharing between the clusters is applied. A correction for the lost energy is also applied depending on the distance of the cluster to the beam pipe.

4.4 Evaluation of Kinematic Variables

4.4.1 Invariant Mass

As it was explained is Section 4.2, the momentum of the charged particles can be obtained from the reconstruction of the information measured at the magnet spectrometer for each event. As the momentum is measured with very high resolution, only this information is used in this analysis to reconstruct the energy of the tracks. The energy of the particles is therefore calculated using the rest mass of the particles and the measured 3-momentum. The 4-momentum of a charged particle is:

$$p = \begin{pmatrix} \sqrt{(m_0 c^2)^2 + (pc)^2} \\ p_x \\ p_y \\ p_z \end{pmatrix},$$

where m_0 is the rest mass of the particle and p, p_x, p_y and p_z are the magnitude of the momentum and its space components.

The invariant mass of a system of two particles is obtained squaring the total 4-momentum following Minkowski rules,

$$s = m_{inv}^2 = \begin{pmatrix} \frac{E_1}{c} + \frac{E_2}{c} \\ p_{1x} + p_{2x} \\ p_{1y} + p_{2y} \\ p_{1z} + p_{2z} \end{pmatrix}^2 = m_1^2 + m_2^2 + 2\left(\frac{E_1}{c} \cdot \frac{E_2}{c} - \vec{p_1} \cdot \vec{p_2}\right).$$

4.4.2 Transverse Momentum

The square of the total transverse momentum of one event is defined as

$$p_t^2 = p^2 - (\ \vec{k} \cdot \vec{p}\ )^2, \tag{4.4}$$

where:

- $\vec{p}$ is the sum of the 3-momenta of the observed decay products.
- $\vec{k}$ is the unitary vector in the direction of flight of the decaying particle and is calculated by using the position of the target and the reconstructed decay vertex position measured at the drift chambers.

For a fully reconstructed event where the momenta of all the decay products are measured, the total transverse momentum must be zero.

4.4.3 Particle Identification

For charged particles, the ratio between the energy measured at the electromagnetic calorimeter and the momentum measured at the magnet spectrometer can be evaluated. This variable is called EOP (E over P),

$$EOP = \frac{E_{LKr}}{p_{spectrometer}} \tag{4.5}$$

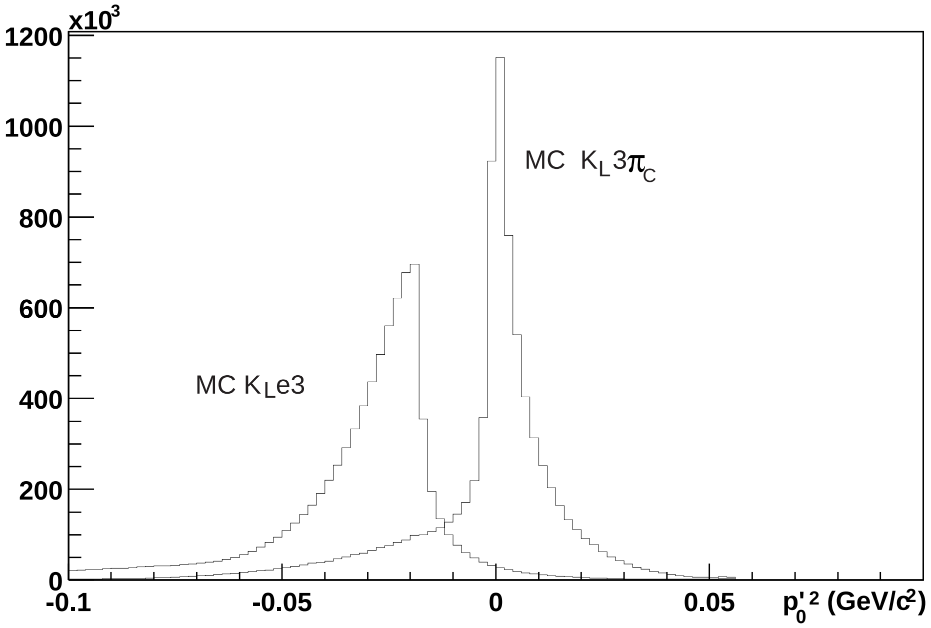

Figure 15: Reconstructed $(p_0\text{'})^2$ variable for MC K_{Le3} and MC $K_{L3\pi_c}$. Both Monte Carlo samples are normalized to the same number of entries.

and it is used for particle identification.
Electrons deposit all their energy in the electromagnetic calorimeter and therefore they have an EOP centered around 1 with a gaussian width of $\sigma = 1,2\%$. On the contrary, pions, protons and other hadrons, have a very broad EOP distribution centered around 0.5 which can eventually also reach the region of $EOP \simeq 1$. Since muons interact very weakly at the electromagnetic calorimeter, they have an EOP very close to 0. See Figure 27 in the next section for more details about this variable.

4.4.4 Closest Distance of Approach between two Tracks

For two well defined tracks it is possible to calculate the closest distance of approach between them. To do that, the space point where the two tracks are closest to one another is calculated (cda-vertex).The cda is thus the distance between the tracks at this point.

4.4.5 The Kinematic Variable $(p_0\text{'})^2$

This variable allows to distinguish between semileptonic neutral kaon decays and $K_L \to \pi^+\pi^-\pi^0$ ($K_{L3\pi_c}$) decays using only the information from the magnet spectrometer. The definition of this variable is

$$(p_0\text{'})^2 = \frac{(m_{K^0}^2 - m_{\pi^0}^2 - m_{\pi^+\pi^-}^2)^2 - 4(m_{\pi^0}^2 m_{\pi^+\pi^-}^2 + p_t^2 m_{K^0}^2)}{4(p_t^2 + m_{\pi^+\pi^-}^2)}, \tag{4.6}$$

where m_{K^0} and m_{π^0} are the masses of the K^0 and the π^0 respectively, $m_{\pi^+\pi^-}$ the invariant mass of the charged particles assuming it is a pair of charged pions, and p_t is the transverse momentum of the event with respect to the direction of flight of the kaon. The variable $(p_0\text{'})^2$ corresponds to the momentum of the kaon in the frame where the longitudinal momentum of the pion pair is zero. In Figure 15, a simulation of this variable for Monte Carlo K_{e3}- and Monte Carlo $K_{L3\pi_c}$-decays can be seen.

5 The Monte Carlo Simulation

The use of Monte Carlo (MC) simulation techniques in this analysis has three purposes:

- It allows to identify and reject background sources by studying and comparing their behavior.
- It permits to access both the reconstructed and the true values of any generated magnitude.
- The acceptance of a decay, i.e. the amount of selected events of one decay with respect to the number of generated events of the same decay within the same energy and z-decay vertex region, can be determined.

There are two different Monte Carlo programs which simulate the NA48 detector, NASIM (NA48 SIMulation) and NMC (New Monte Carlo). The program NASIM [30] is based on the GEANT package [31] and uses an exact tracking simulation of the charged particles. NMC [32, 33] is a much faster program which does not perform such a detailed reconstruction of the drift chambers and therefore provides more statistics within shorter times. In this analysis the NASIM program was used to simulate neutral kaons decays, whereas NMC was used to study Λ decays.

5.1 Simulation of Decays

The momenta of the decay products are generated according to phase space and it can afterwards be weighted by the corresponding matrix element. The calculation of the 4-momentum of the decay products is done in the rest frame of the decaying particle and then a Lorentz transformation gives the values in the lab-frame. After this, the flight of the particles through the detector is simulated and all the possible interactions with the detector components (pair conversions, bremsstrahlung, multiple scattering, etc.) are taken into account. The resolution of each subdetector must also be implemented in the simulation.

The Monte Carlo events are generated in COmPACT-format and then converted into ROOT-files (see Sections 3.9.4 and 4.4), in this way, the same reconstruction program which is used for the data analysis can also be used for the Monte Carlo events.

5.1.1 Simulation of Neutral Kaons

Kaons can be generated within a free energy and z-decay vertex range. In order to generate the energy and momentum of neutral kaons, the production spectrum of charged kaons [34] is used together with a small correction which accounts for the experimentally observed distribution. The production spectrum is given by

$$\begin{aligned}\frac{d^2N}{dp_K d\Omega} = \frac{0.4p_K^2}{4p_0}\Big[1.30 \cdot e^{\left(-8.5\cdot\frac{p_K}{p_0}-3.0\cdot p_K^2\Phi^2\right)} &+ \\ +4.35 \cdot e^{\left(-13.0\cdot\frac{p_K}{p_0}-3.5\cdot p_K^2\Phi^2\right)}\Big]& \\ \cdot e^{(4.2+0.053\cdot p_K)} &+ 0.016, \qquad (5.1)\end{aligned}$$

where p_K is the momentum of the kaon, $p_0 = 450$ GeV/c is the momentum of the protons from the SPS and $\Phi = 4.2$ mrad is the production angle at the K_S target.

The decay spectrum depends on the lifetime of the decaying particle. It can be obtained by weighting the production spectrum of equation (5.1) with the decay probability distribution expressed as

$$\frac{d^2N}{dzdE} = e^{\frac{-z}{\lambda}}, \qquad (5.2)$$

being $\lambda = \gamma\beta c\tau$ the mean free path and z the distance the particle flies before it decays. After this weighting, an integration over the desired decay range must be performed.

5.1.2 Parameters of the Simulation

The decay spectrum of the simulated decays is generated as a function of the energy and the z-decay vertex position.

- The momentum of the decaying particles is generated within

$$40 \text{ GeV} \leq p_{K^0,\Lambda} \leq 220 \text{ GeV}.$$

- The decay region is limited to

$$4 \text{ m} \leq z_{decay\ vertex} \leq 60 \text{ m}.$$

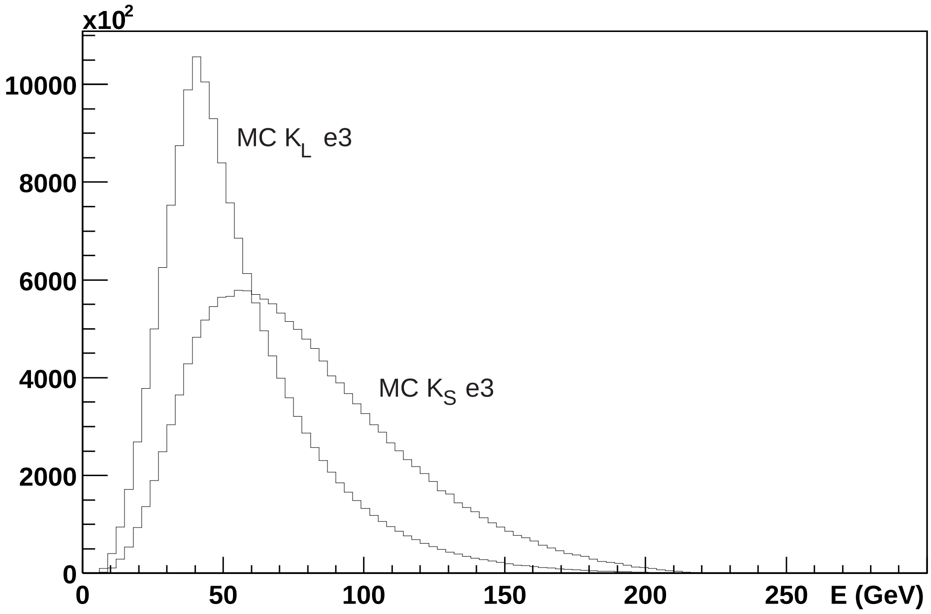

Figure 16: Energy spectrum of Monte Carlo K_{Le3}- and Monte Carlo K_{Se3}-decays. Same number of entries in both channels.

5.2 K_{e3} Monte Carlo Simulation

The NA48 Monte Carlo simulation programs do not provide the interference between two different decays, they only generate single decay channels of a given particle. K_{Se3} and K_{Le3} decays are kinematically equivalent, they only differ in the decay probability distributions. In Figures 16 and 17, the generated kaon energy spectrum and the z-decay vertex distribution of kaons are shown for both kinds of Monte Carlo K_{e3} events. In these figures, the simulations are normalized to the same number of entries and are generated from the K_S target with the same simulation parameters. Differences in the distributions of K_S- and K_L-decays can be explained by equation (5.2) considering the dependence of the decay probability on the energy, lifetime and decay position of the particles.

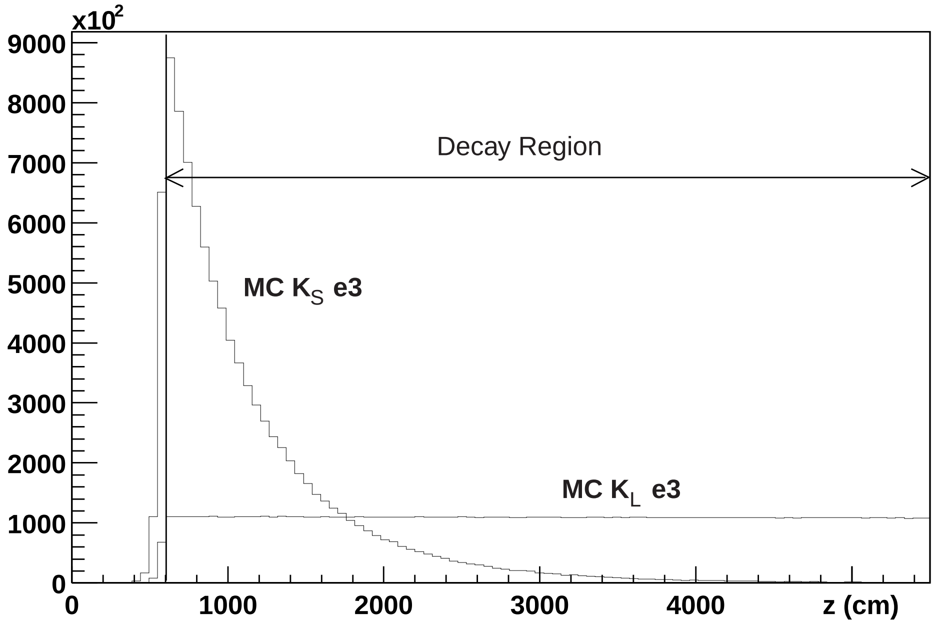

Figure 17: Decay vertex distributions of Monte Carlo K_{Le3}- and Monte Carlo K_{Se3}-decays. Same number of entries in both channels. Long-lived kaons give an almost flat contribution in the decay region, which corresponds to about 8 cτ_S and 0.01 cτ_L.

6 Selection of Events

The most precise measurement of the BR($K_S \to \pi^{\pm} e^{\mp} \nu_e$) performed up to now [2] shows that the K_S-meson decays into this channel with a probability of $(6.91 \pm 0.37) \times 10^{-4}$. In the case of K_{Le3}-decays the situation is completely different. The branching fraction is BR($K_L \to \pi^{\pm} e^{\mp} \nu_e$) $= (38.78 \pm 0.28)\%$ [3], which is much higher than for K_{Se3}-decays and it has exactly the same signature (the same signal) but different lifetime.

K_{e3}-decays are three-body decays with two charged tracks which can interact electromagnetically in the detector, and one neutral particle, an electron-neutrino, which does not interact at all. There are some other $K_{S,L}$- and Λ-decays produced at the target which have a similar signature and lifetime and higher decay probability and therefore have to be studied and simulated in order to be rejected from the final data sample. $K_S \to \pi^+ \pi^-$, $\Lambda \to p\ \pi^-$, $\Lambda \to p\ e^-\ \overline{\nu_e}$, and their charge conjugate states are some of the most important backgrounds to be expected since they also have two charged tracks as a signal in the detector.

6.1 The Data Sample

As explained in Section 3.10, from the original data sample of the '1999 K_S High Intensity Run' only events which passed both the Hyperon Level 1 Pre-Trigger and the Hyperon Level 2 Trigger conditions are used in this analysis. In addition to this requirement, in order to have exactly the same trigger conditions for all data, only data collected in run number 2 are included in the final sample. In run number 2, the Hyperon Level 2 Trigger was used to remove $K_S \to \pi^+ \pi^-$ events by applying a cut on the invariant mass and the momentum ratio of the two charged tracks selected by the Level 1 Pre-Trigger. Events with a reconstructed invariant mass within $|m_{\pi^+\pi^-} - m_{K^0}| < 25 - 30$ MeV/c^2 and a momentum ratio between $\frac{1}{4-5} < \frac{p_+}{p_-} < 4 - 5$ were not accepted by this trigger (see Figure 18). Downscaling factors between 4 and 8 (one event out of four triggered events is accepted) had to be applied in order to reduce the high rate of the trigger. In Table 6 the runs used in this analysis are listed [25].

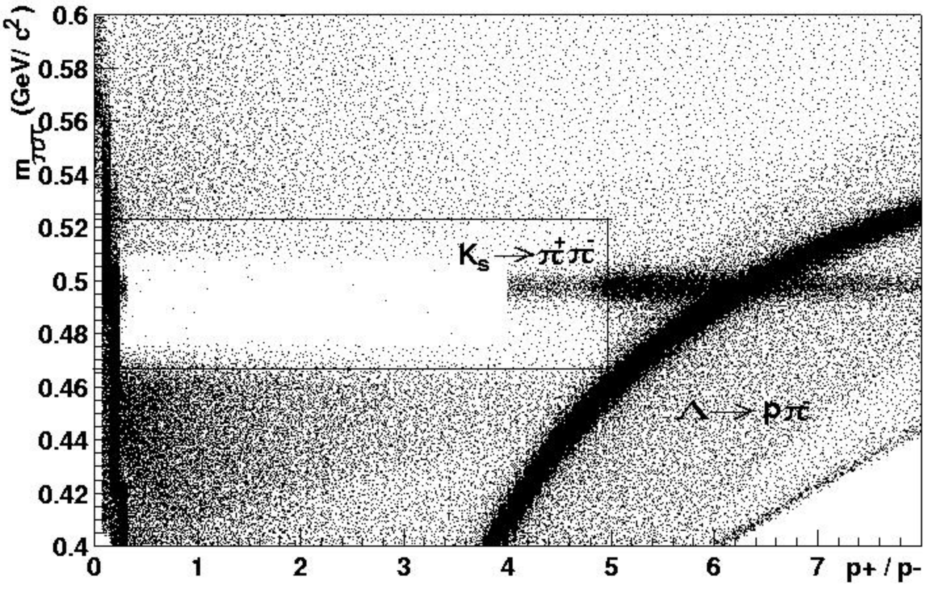

Figure 18: The Hyperon-Trigger. Reconstructed momentum ratio of two tracks vs invariant mass under $\pi^+\pi^-$ assumption. The central empty region around the kaon mass is produced by this trigger, events within this region are eliminated. The dark curved region between $R_p = 4$ and $R_p = 8$ corresponds to $\Lambda \rightarrow p\ \pi^-$ decays, whereas the dark region with $\frac{p+}{p-} < \frac{1}{4}$ contains $\overline{\Lambda} \rightarrow \overline{p}\ \pi^+$ decays. The empty region between $R_p = 6$ and $R_p = 8$ is forbidden by kinematics.

Run	Q1-downsc.	Hyp.-donsc.	$m_{\pi^+\pi^-}$ window (MeV/c^2)	$\frac{p+}{p-}$ window	Bursts
9303	128	8	$\lvert m_{\pi^+\pi^-} - m_{K^0}\rvert < 25$	$1/4 < R_p < 4$	27
9304	128	8	$\lvert m_{\pi^+\pi^-} - m_{K^0}\rvert < 25$	$1/4 < R_p < 4$	296
9305	128	8	$\lvert m_{\pi^+\pi^-} - m_{K^0}\rvert < 30$	$1/5 < R_p < 5$	485
9306	128	8	$\lvert m_{\pi^+\pi^-} - m_{K^0}\rvert < 30$	$1/5 < R_p < 5$	22
9307	128	8	$\lvert m_{\pi^+\pi^-} - m_{K^0}\rvert < 30$	$1/5 < R_p < 5$	56
9308	128	5	$\lvert m_{\pi^+\pi^-} - m_{K^0}\rvert < 30$	$1/5 < R_p < 5$	69
9309	128	6	$\lvert m_{\pi^+\pi^-} - m_{K^0}\rvert < 30$	$1/5 < R_p < 5$	816
9311	128	6	$\lvert m_{\pi^+\pi^-} - m_{K^0}\rvert < 30$	$1/5 < R_p < 5$	227
9312	64	6	$\lvert m_{\pi^+\pi^-} - m_{K^0}\rvert < 30$	$1/5 < R_p < 5$	381
9313	64	6	$\lvert m_{\pi^+\pi^-} - m_{K^0}\rvert < 30$	$1/5 < R_p < 5$	900
9315	64	6	$\lvert m_{\pi^+\pi^-} - m_{K^0}\rvert < 30$	$1/5 < R_p < 5$	1032
9318	64	4	$\lvert m_{\pi^+\pi^-} - m_{K^0}\rvert < 30$	$1/5 < R_p < 5$	137
9320	64	5	$\lvert m_{\pi^+\pi^-} - m_{K^0}\rvert < 30$	$1/5 < R_p < 5$	1821
9321	64	5	$\lvert m_{\pi^+\pi^-} - m_{K^0}\rvert < 30$	$1/5 < R_p < 5$	2863

Table 6: Conditions of the Hyperon-Trigger during run number 2.

6.2 The Selection of Events

The cuts applied to select K_{e3} candidates are described in this section. All cuts are applied to both data and Monte Carlo K_{Le3} events in order them to fulfill the same requirements. All cuts and figures are explained in the following sections in the same order in which they are applied in the analysis.

Most of the selection variables used here (cda, EOP, invariant mass of a system of two particles, etc.) were already explained in Section 4.4 and make use of the information provided by the electromagnetic calorimeter and the magnet spectrometer. The reconstructed information from the different subdetectors concerning the events (number of tracks, momentum, energy of the clusters, vertices, etc.) is available in COmPACT format already provided by the Level 3 Trigger. Nevertheless, the final analysis format are ROOT-Trees [28] with only the relevant information for the analysis. This allows to reduce the size of the data sample from 100 GByte to 10 GByte and it is possible to run over it within hours [29].

6.2.1 Z-Decay Vertex Range

The lower limit of the selected z-decay vertex region is defined by the position of the K_S target (0 cm), while the upper limit is $z = 4500$ cm. This region contains about 7.5 K_S-lifetimes ($< E_{kaon} > \approx 110$ GeV) and therefore 99.9% of the K_S-decays.

6.2.2 The Energy Range

It is required that the total energy of the two charged tracks $E_{\pi e}$ is higher than 50 GeV and less than 215 GeV. A minimum energy of 50 GeV is chosen to ensure a 100% efficiency of the Level 1 Pre-Trigger in the reconstruction of low energy events. The upper limit on $E_{\pi e}$ is imposed by the maximum energy in the energy spectrum of the produced kaons.

6.2.3 Pre-selection Cuts

Two Tracks in the Drift Chambers
This requirement was already imposed by the Level 1 Pre-Trigger on the data.

Total Charge Equal Zero
Two charged tracks with opposite charge and opposite deviation in the magnet spectrometer are required.

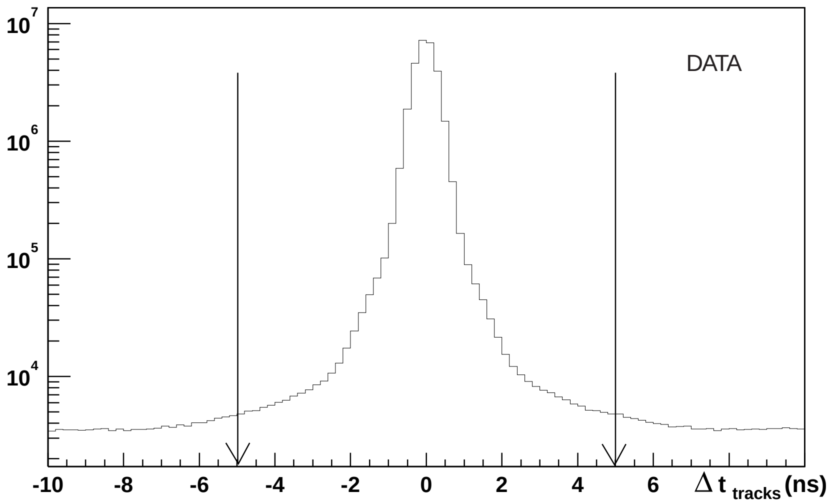

Figure 19: Time difference between charged tracks at the hodoscope for charged particles. The y-axis is in logarithmic scale.

One Reconstructed Vertex
This condition implies that the reconstruction software must find a region where the two tracks are closer to one another.

Time Difference between the Tracks
Charged particles coming from the decay of the same particle should enter the hodoscope for charged particles at the same time. It is asked that the time difference between the tracks (Δt_{tracks}) is less than 4.5 ns (see Figure 19). This cut is meant to eliminate all events with tracks coming from a different decay and accidental events. This cut is not applied to Monte Carlo events because no time references are implemented in the Monte Carlo simulation programs.

Hyperon-Trigger.
In order to increase the efficiency of the Hyperon-Trigger, the following events are rejected:

- events with a reconstructed invariant mass within $|m_{\pi^+\pi^-} - m_{K^0}| < 30$ MeV/c^2 under a $\pi^+\pi^-$ assumption,
- and with a momentum ratio between $\frac{1}{5} < \frac{p_+}{p_-} < 5$.

The new requirements harden the previous requirements and produce the rejection of events inside the black box plotted in Figure 18 and centered around the kaon mass.

6.2.4 Geometry Cuts

X-Decay Vertex Coordinate

The collimated products from the pN collisions at the target are strongly boosted in the z direction. No deviations along the x-axis are expected, and therefore only decays with an x-decay vertex position within $|x| < 2$ cm are accepted. The selected region can be seen in Figure 20. In this figure, the region of $z < 600$cm contains events not well reconstructed, collimator scattering of neutral particles and decays of short lived particles which happen before the collimator. In Figures 22 and 24 the x-decay vertex position is showed for the Monte Carlo K_{e3} events. The number of entries is not normalized in these plots.

Y-Decay Vertex Coordinate

Only particles produced at the K_S target ($y = 7.2$ cm) which decay during their way to the center of the detector are accepted. This means that only events with an angle of about 0.6 mrad between their direction of flight and the z-axis are studied. The selected region is reduced to:

$$6.0 \times \left(1 - \frac{z(\text{cm})}{12100}\right) < y(\text{cm}) < 9.5 \times \left(1 - \frac{z(\text{cm})}{12100}\right) \tag{6.1}$$

This cut defines the decay region and reduces the amount of background coming from the scattering of particles at the collimators (from both the former K_L beam and the K_S beam, see Figure 21). Since the K_L collimator of the former K_L beam was not removed from the experimental setup, also scattering of particles coming from the K_S target can be observed around this collimator (region of $300 < z$ (cm) < 600 and $-3 < y$ (cm) < 3). Figures 23 and 25 show the y-decay vertex position of the Monte Carlo simulations. These distributions are not normalized.

Closest Distance of Approach between the Tracks

The closest distance of approach between the tracks (see Section 4.4.4) must be less than 2.5 cm in order to have a well defined vertex.

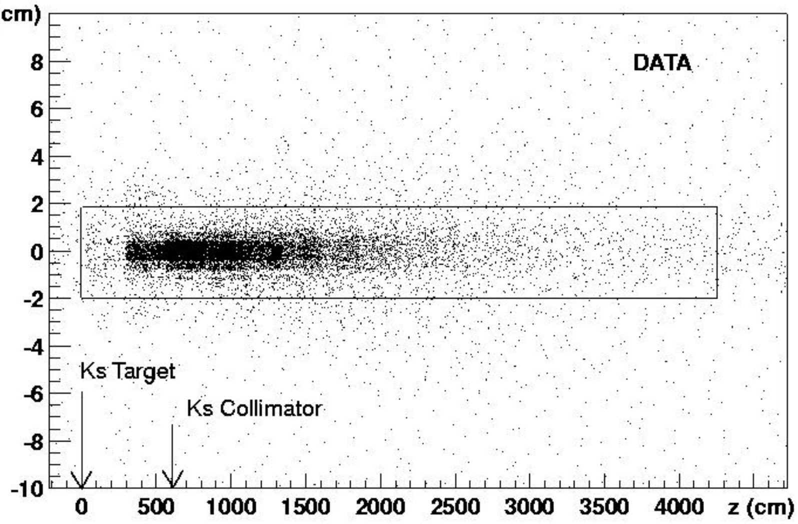

Figure 20: Reconstructed x-decay vertex vs z-decay vertex position. Events with $|x| < 3$ cm and $0 < z$ (cm) < 600 scatter at the K_S collimator. Only events inside the marked box are selected.

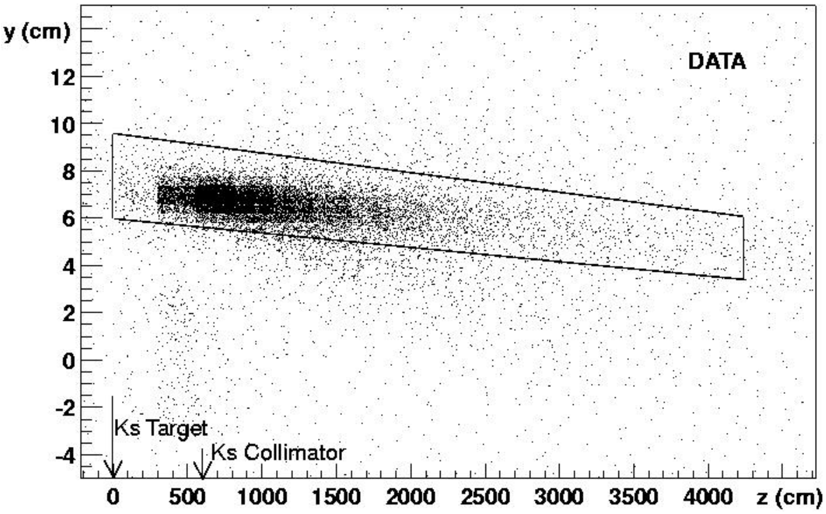

Figure 21: Reconstructed y-decay vertex vs z-decay vertex position. The scattering of particles at the collimator of the former K_L beam and at the K_S collimator can be observed between $0 < z$ (cm) < 600. Only events inside the marked box are selected.

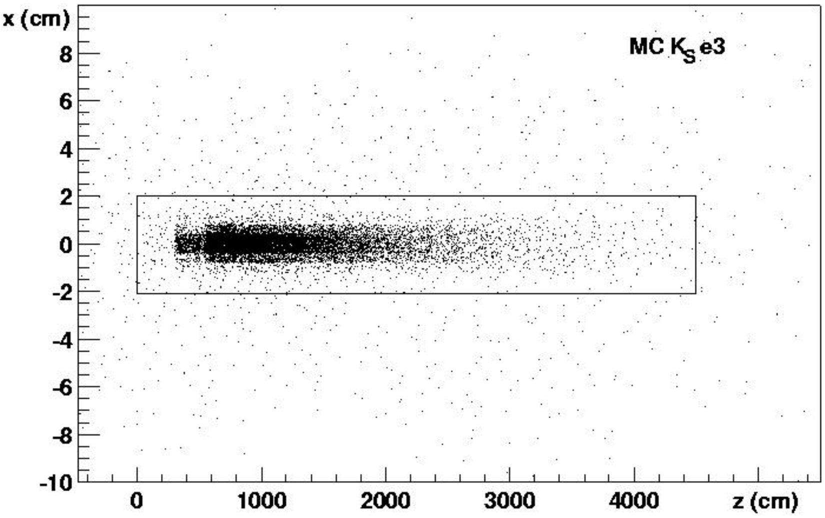

Figure 22: Reconstructed x-decay vertex vs z-decay vertex position of Monte Carlo K_{Se3}-decays. Only events in the marked region are selected.

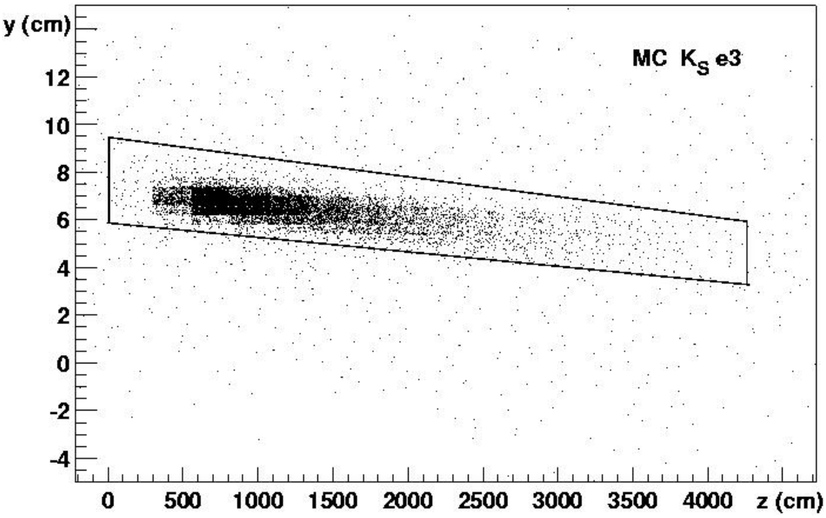

Figure 23: Reconstructed y-decay vertex vs z-decay vertex position of Monte Carlo K_{Se3}-decays. Only events in the marked region are selected.

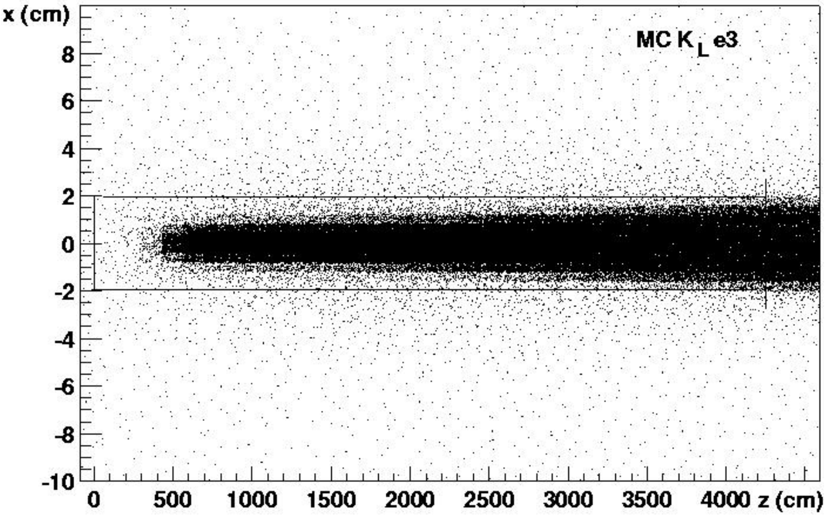

Figure 24: Reconstructed x-decay vertex vs z-decay vertex position of Monte Carlo K_{Le3} decays. Only events in the marked region are selected.

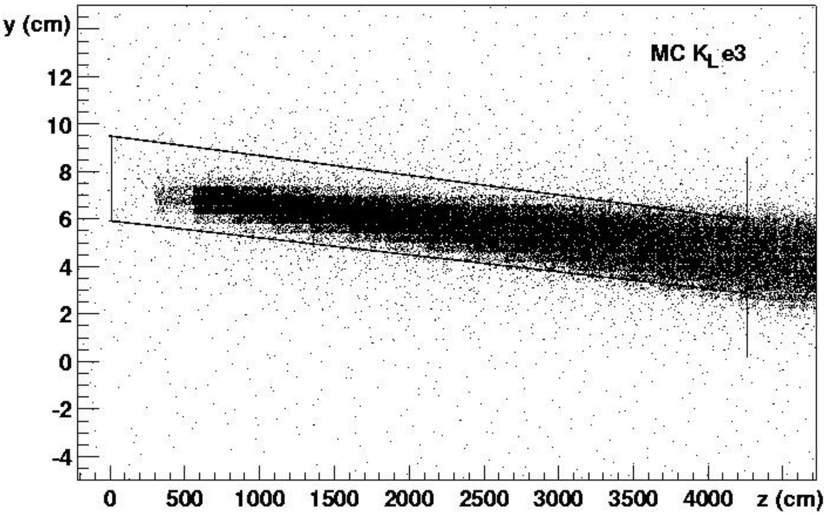

Figure 25: Reconstructed y-decay vertex vs z-decay vertex position of Monte Carlo K_{Le3}-decays. Only events in the marked region are selected.

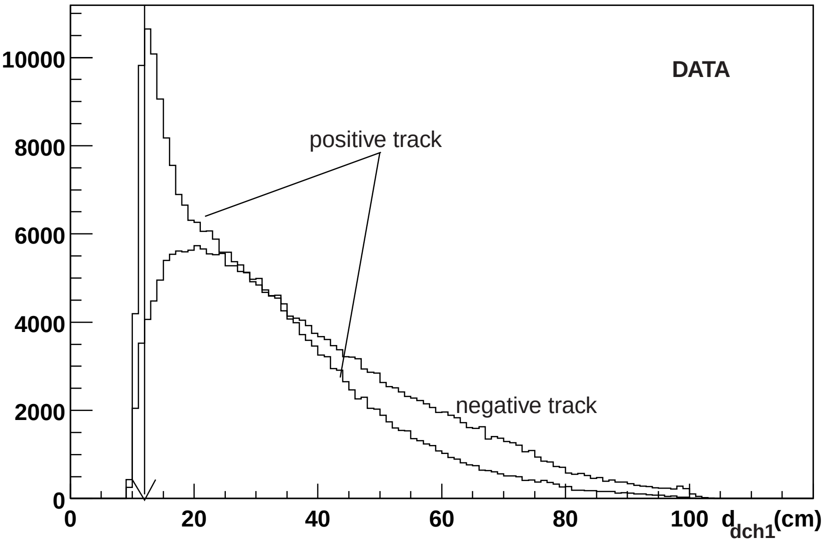

Figure 26: Reconstructed radial distance of the tracks to the center of the beam pipe at the first drift chamber.

Distance of the Tracks to the Beam Pipe

The drift chambers reach the 100% of efficiency for distances higher than 12 cm from the center of the beam pipe [25]. For this reason only tracks with a radial distance to the center of the beam pipe (d_{dch}) higher than 12 cm in all the drift chambers are accepted.

In Figure 26 the distance to the center of the beam pipe in DCH1 is shown for the tracks. Differences in both tracks are due to the higher proton contribution to the positive track. These protons are originated in Λ decays such as $\Lambda \rightarrow p\pi^-$ and $\Lambda \rightarrow pe^-\overline{\nu_e}$ and due to their higher boost in the z-direction travel closer to the beam pipe.

6.2.5 Selection of K_{e3} Events and Background Rejection

Identification of Electrons/Positrons and Pions

Electrons, positrons and photons deposit all their energy in the LKr electromagnetic calorimeter creating electromagnetic showers. Hadrons can interact in many different ways in the LKr calorimeter and usually they do not lose all the energy in there.

As already explained in Section 4.4.3, it is possible to distinguish the products involved in one decay by looking at the energy deposited by them in the electromagnetic calorimeter and comparing it to the measurement of the momentum provided by the magnet spectrometer.

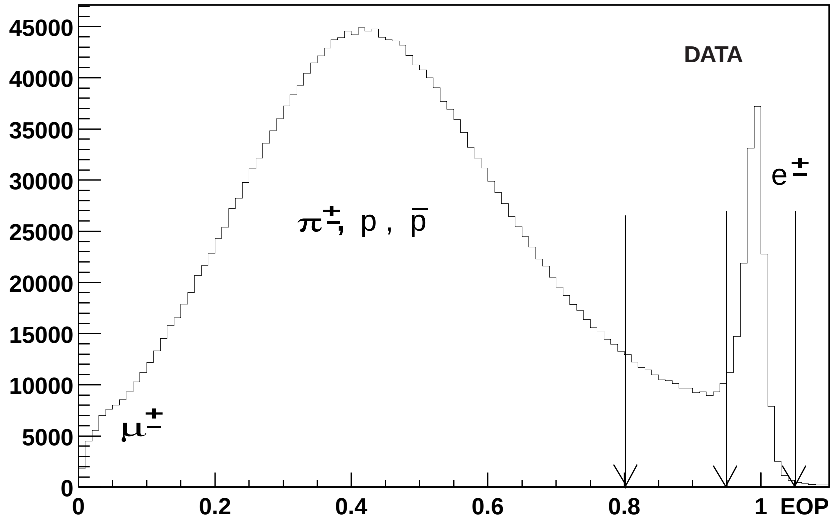

Figure 27: Ratio between energy deposited at the electromagnetic calorimeter and momentum measured at the spectrometer.

To select both K_{e3} charge modes, each event is asked to have two tracks with opposite charge where:

- the track associated to the π^+, π^- should have:

$$0 < EOP|_\pi < 0.80, \tag{6.2}$$

- and the track associated to the e^-, e^+ should have:

$$0.95 \le EOP|_e < 1.10. \tag{6.3}$$

As can be seen from Figure 27, the two selected regions do overlap and therefore one can still misidentify hadrons with high EOP as electrons.

Hadron Showers in the Electromagnetic Calorimeter

Hadron showers can be created due to inelastic collisions of the hadrons produced in the decays when they interact with the electromagnetic calorimeter. Primary charged particles resulting from these collisions can separate from the main shower and build secondary showers which can be misidentified as several primary ones.

In order to consider the possibility of having hadron showers coming from the incoming pions, more than two clusters at the LKr electromagnetic calorimeter are allowed if:

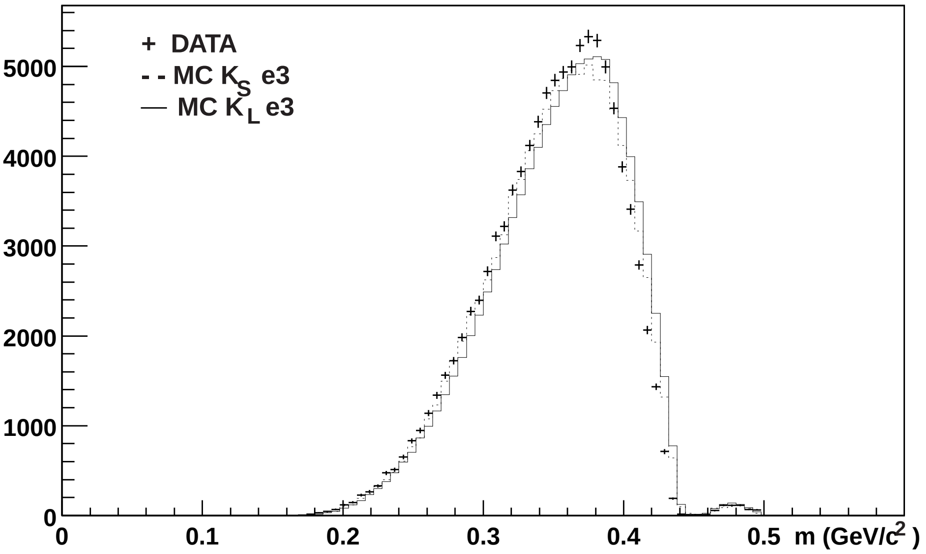

Figure 28: Reconstructed invariant mass of the pion-electron system. The empty region around 0.45 GeV is caused by the Hyperon-Trigger for the rejection of $K_S \to \pi^+\pi^-$ decays.

- the distance between the hadron shower and any secondary shower is less than 25 cm,
- and the energy of the secondary shower is less than 6 GeV [35].

Invariant Mass of the Decay Products

The invariant mass of the decay products has to be within the kinematic limits for K_{e3}-decays (see Section 4.4.1):

$$m_\pi + m_e < m_{\pi e} < m_{K^0} \tag{6.4}$$

The reconstructed invariant mass of the charged tracks under a pion-electron assumption is shown in Figure 28. The empty region around 0.45 GeV is due to the cut on the reconstructed invariant mass of the $K_S \to \pi^+\pi^-$ decays done by the Hyperon Level 2 Trigger (see Figure 18).

Conversion Pairs

The decay products coming from some decays can produce e^+e^- pairs when the photons resulting from these decays get in contact with the material from the detector. Conversion pairs which happen at the beginning of the detector can still be measured and need to be rejected. Since conversions are originated in the detector itself, the tracks are still very close to one another when they reach the first drift chamber and can be identified.

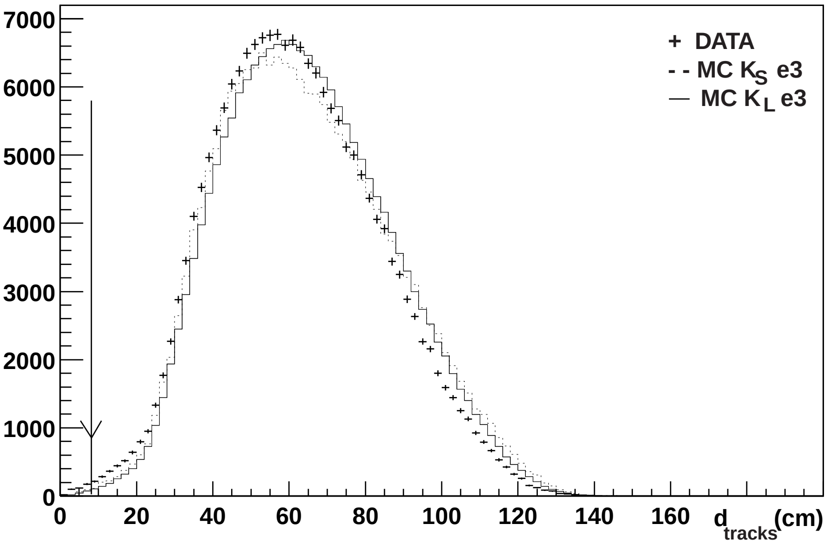

Figure 29: Reconstructed distance between the tracks at the first drift chamber.

In order to eliminate background coming from conversion pairs, events with a distance between the two charged tracks at the first drift chamber (d_{tracks}) less than 7 cm are rejected (see Figure 29). This cut is applied for the sake of safety, since most of the e^+e^- pairs are already filtered by the EOP cut.

Minimum Momentum of the Tracks

The minimum momentum of the track associated to the electron (positron) has to be higher than 5 GeV, while the minimum momentum of the track associated to the pion has to be higher than 8 GeV. In this way, low energy events for which the energy resolution is worse are rejected. In Figure 30 the momenta of both tracks are shown. In these picture can again be observed the higher boost of the track associated to the pions.

Rejection of $K_S \to \pi^+\pi^-$ Events

The probability of this decay is $\mathrm{BR}(K_S \to \pi^+\pi^-) = 68.61 \pm 0.28\%$. It is a thousand times more likely than a K_{Se3}-decay. Since this decay has only two charged tracks which can be observed at the detector, the signature is similar to the one of a K_{e3}-decay. The Hyperon-Trigger only removed those $K_S \to \pi^+\pi^-$ decays with a momentum ratio between $\frac{1}{4-5} < \frac{p_+}{p_-} < 4-5$. A new harder cut on the invariant mass of the two pions system permits to eliminate these decays completely from the data sample. Events with $|m_{\pi^+\pi^-} - m_{K^0}| < 4\sigma$ are rejected, with $4\sigma = 12.4$ MeV (see Figure 31).

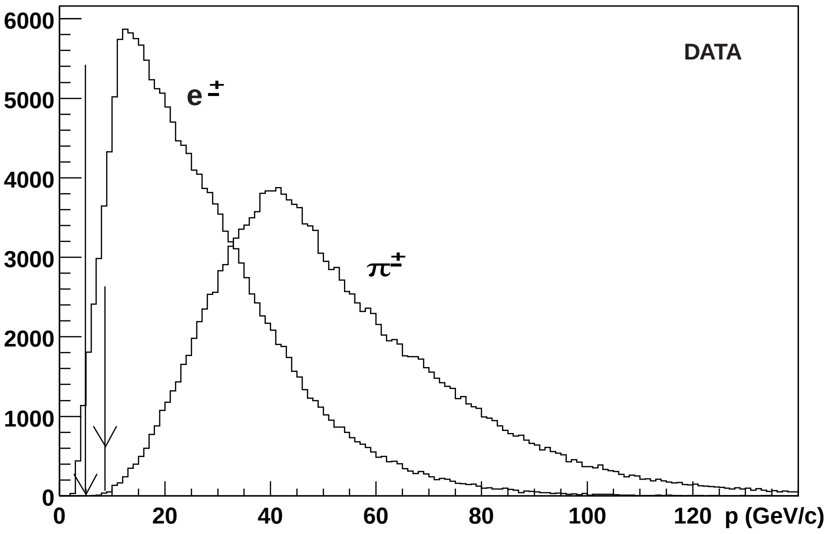

Figure 30: Reconstructed momentum of the two tracks.

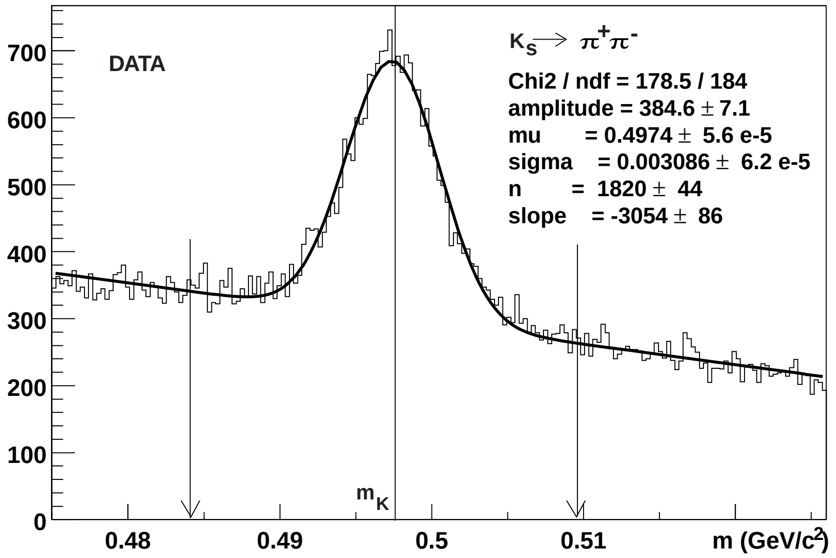

Figure 31: Reconstructed invariant mass of the two tacks under $\pi^+\pi^-$ assumption. Events distributed around m_{K^0} are rejected.

Rejection of $\Lambda \to p\ \pi^-$ Events

Since the lifetime of Λ-hyperons is very similar to the K_S-lifetime ($\tau_\Lambda = (2.632 \pm 0.020) \times 10^{-10}$ s [3]), Λ-decays lie also in the same z-decay vertex region as K_S-decays and therefore constitute an important source of background for K_S-decays.

Like in the previous case, this decay has also a two tracks signature, and a branching fraction of BR($\Lambda \to p\ \pi^-$) $= 63.9 \pm 0.5\%$ [3].

In order to reject $\Lambda \to p\ \pi^-$ decays from the data sample, the following events are removed:

$$|m_{p\ \pi^-} - m_\Lambda| < 4\sigma, \tag{6.5}$$

where $4\sigma = 3.6$ MeV (see Figure 32).

Rejection of $\overline{\Lambda} \to \overline{p}\ \pi^+$ Events

This decay is the charged conjugate state of the previous one. The branching fraction is exactly the same as in the Λ-decay case, but since the probability of producing a $\overline{\Lambda}$ is lower (see Section 2.5.3), the amount of $\overline{\Lambda}$ decays is also smaller.

In order to remove $\overline{\Lambda} \to \overline{p}\ \pi^+$ decays, events with a reconstructed invariant mass of the two tracks under $\pi^+\ \overline{p}$ assumption within:

$$|m_{\overline{p}\ \pi^+} - m_{\overline{\Lambda}}| < 4\sigma = 3.7\text{MeV} \tag{6.6}$$

are rejected (see Figure 33).

Rejection of $K_L \to \pi^+\pi^-\pi^0$ Events

This decay has a probability of $(12.55 \pm 0.20)\%$. In order to accept this decay as K_{e3}-event, the decay products of the $\pi^0 \to \gamma\gamma$ decay must be lost, i.e. not measured by the detector.

A cut on the $(p_0')^2$ variable (Section 4.4.5) is applied in order to reject this background. All events with: $(p_0')^2 > -0.01$ (GeV/c)^2 are eliminated.

Rejection of $\Lambda \to p\ e^-\overline{\nu}_e$ and $\overline{\Lambda} \to p\ e^+\nu_e$ Events

The branching fraction of this decay is:

$$BR(\Lambda \to p\ e^-\overline{\nu}_e) = (8.32 \pm 0.14) \cdot 10^{-4} \quad [3],$$

which means that it is about 800 times more unlikely than the $\Lambda \to p\ \pi^-$ decay. However, as it has got exactly the same signature as the K_{e3}-decays, and therefore it constitutes a very important source of background.

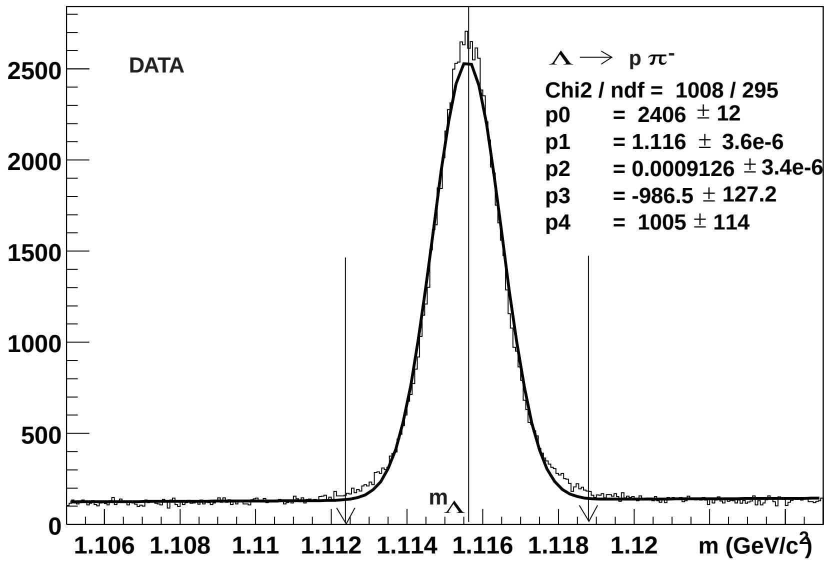

Figure 32: Reconstructed invariant mass of the two tacks under $p\ \pi^-$ assumption. Events distributed around m_Λ are rejected.

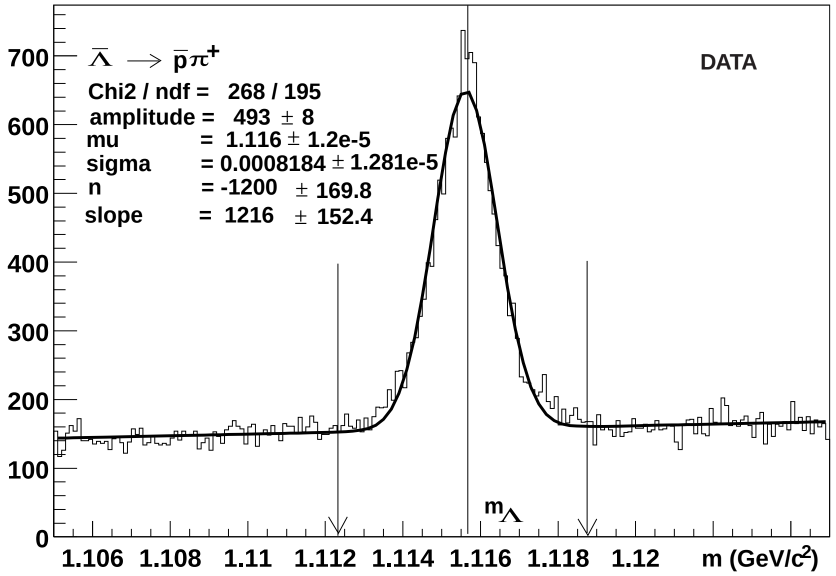

Figure 33: Reconstructed invariant mass of the two tacks under $\overline{p}\ \pi^+$ assumption. Events distributed around m_Λ are rejected.

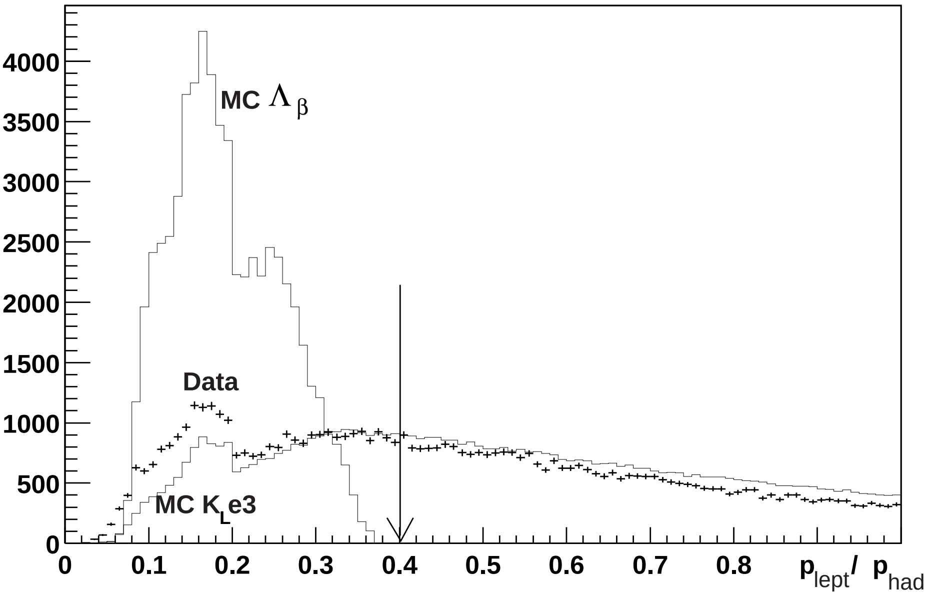

Figure 34: Reconstructed $\frac{p_{lept}}{p_{had}}$ of MC K_{Le3}, MC Λ_β and data. Monte Carlo samples are normalized to the number of data.

These decays, also called 'lambda (antilambda) beta decays' ,Λ_β-decays ($\overline{\Lambda}_\beta$-decays), can be distinguished from K_{e3}-decays in the momentum ratio of the two charged tracks. For a given energy of the hyperon, the proton (antiproton) always takes a much higher momentum than the electron (positron) due to its higher mass (higher boost), being this difference much more pronounced than in the case of pions and electrons (positrons) from K_{e3}-decays.

A cut is applied on the ratio between the momentum of the lepton and the momentum of the hadron, being events with $\frac{p_{lept}}{p_{had}} < 0.4$ rejected. In Figure 34, a comparison between the momentum ratio of Monte Carlo Λ_β-decays, Monte Carlo K_{Le3}-decays, and data is shown. Monte Carlo samples are normalized to the number of data.

Scattering of Particles at the Collimator

The K_S beam is not a perfectly well defined beam line but it is surrounded by a 'halo'. For this reason, it can suffer scattering with the walls of the collimator when passing through it. Some of the events which scatter at the collimator can be identified by their high transverse momentum. In Figure 35 it is represented the z-decay vertex position versus the transverse momentum. As can be seen in this figure, there is an excess of data with high transverse momentum exactly at the collimator position.

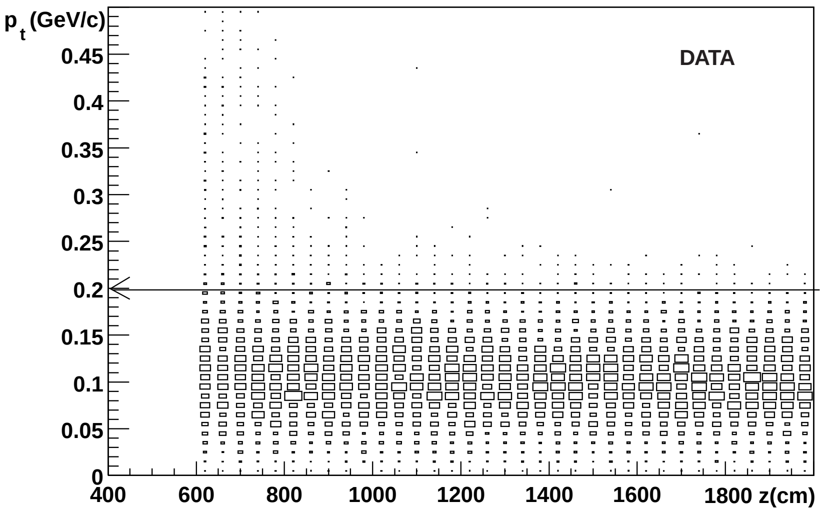

Figure 35: Reconstructed z-decay vertex position vs transverse momentum.

In order to avoid events with high transverse momentum, all events with $p_t > 0.2 GeV$ are rejected.

6.2.6 Background Estimation

In Table 7 the main decays which can appear as background sources are listed. The number of data and background events after each cut and the global acceptances for each one of those decays can be seen in this table. The global acceptance is defined as the ratio between the number of reconstructed and generated events with a z-decay vertex position $z \epsilon [0, 4500]$ cm and energy $E_{\pi e} \epsilon [50, 215]$ GeV.

As can be seen from the table, using the branching fractions given in Table 4 and considering the fact that in this run a total number of about 3×10^8 K_S decays [24] and 18×10^6 $\Lambda \rightarrow p\ \pi^-$ [1] decays were observed in the decay region, no remaining background contribution is expected from any of the decays listed in Table 7.

A background contribution arising from the scattering of neutral particles at the collimator is still expected. After the cut on the transverse momentum events with high-p_t are removed from the data sample (see Figure 35).

---

[1] The number of $\Lambda \rightarrow p\ \pi^-$ decays is evaluated by using all the data collected during this run and reconstructing the invariant mass of this decay.

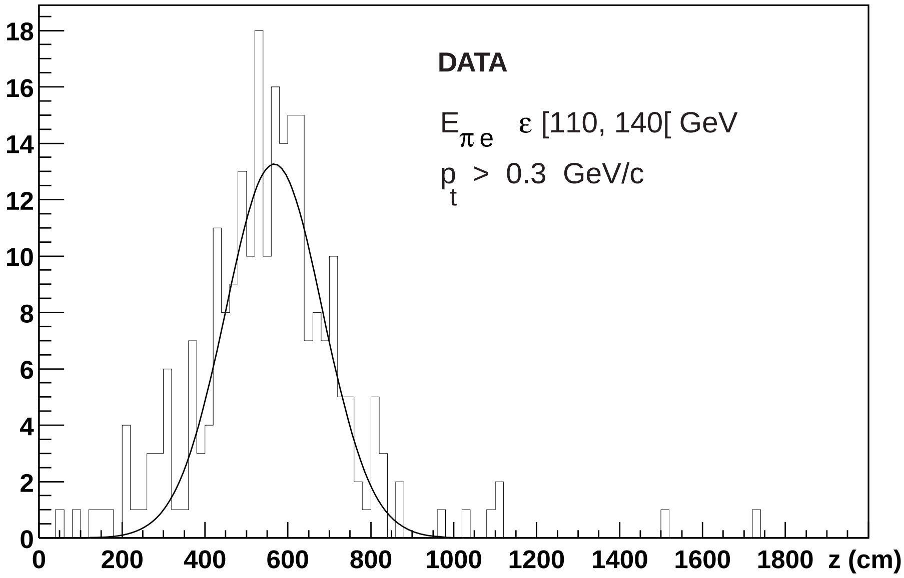

Figure 36: Reconstructed z-decay vertex distribution of high-p_t events.

However, there are also events which scatter at the collimator and get low transverse momentum similar to the one expected for K_{e3}-events. The amount of these 'low-p_t' events can be estimated by using high-p_t events decaying at the collimator as a control region.

A gaussian fit to the z-decay vertex distribution of the high-p_t events is performed depending on the energy of the pion-electron system (see Figure 36 for the case of $110 < E_{\pi e} < 140$GeV). From these fits it is found that the mean and the width of the gaussians do not depend on the energy bin.

In order to quote the amount of low-p_t events which scatter at the collimator, it is assumed that they are gaussian distributed around the collimator with the same mean and width as the high-p_t events, but with different heights. The ratio between the number of low- and high-p_t events is supposed to be constant for all the energy bins (see Section 7.1).

6.2.7 Signal Acceptance

In Table 8 the effect of all the cuts on the data and Monte Carlo signal events is shown together with the global acceptances of the Monte Carlo. The z-decay vertex region is defined to lie in $z \epsilon [0, 4500]$ cm.

Cut	$K_S \to \pi^+ \; \pi^-$	$\Lambda \to p \; \pi^-$	$\Lambda \to p \; e^- \; \nu_e$	$K_{L \; 3\pi_c}$
Entries	2129758	3810224	6356560	1201887
2tracks	1573215	425345	516464	646589
$Q_T = 0$	1566520	424864	512401	636500
1vertex	1561586	424747	512395	632375
Hyp.-Trigg.	168281	423730	489061	632303
Δt	168281	423730	489061	632303
$E_{\pi e}$	157985	402325	473621	344513
z-vtx.	151928	386069	471136	329170
x, y, cda	121059	364483	464052	284371
d_{dch}	74913	156114	227875	216070
EOP	15	43	211415	472
clusters	9	35	164887	69
$m_{\pi e}$	9	35	164642	69
d_{tracks}	9	35	164296	69
p_e, p_π	9	35	163864	69
$m_{\pi^+\pi^-}$	9	30	148536	69
$m_{p \; \pi^-}$	9	0	126197	69
$m_{\overline{p} \; \pi^+}$	9	0	126197	69
$(p_0')^2$	9	0	115719	7
$p_</p_>$	5	0	0	4
p_t	5	0	0	3
α	$2.34 \cdot 10^{-6}$	0%	0%	$2.5 \cdot 10^{-6}$

Table 7: List of the main possible background decays, number of entries after each cut and global acceptances.

Cut	Data	$K_S \to \pi^\pm e^\mp \nu_e$	$K_L \to \pi^\pm e^\mp \nu_e$
Entries	32398500	4244692	8240891
2tracks	32398500	2828954	5238724
$Q_T = 0$	32398500	2813770	5207500
1vertex	32398500	2807622	5197376
Hyp.-Trigg.	31951895	2434263	4410987
Δt	28093410	2434263	4410987
$E_{\pi e}$	23717647	2104968	3084826
z-vtx.	23512704	2092933	2939945
x, y, cda	19683114	2012280	2535981
d_{dch}	15581060	1798738	2270934
EOP	250228	1536893	1800185
clusters	193116	1195438	1428407
$m_{\pi e}$	191644	1195299	1428219
d_{tracks}	191316	1194609	1427535
p_e, p_π	189514	1189106	1416947
$m_{\pi^+\pi^-}$	181763	1165093	1388125
$m_{p\ \pi^-}$	169435	1146392	1367013
$m_{\overline{p}\ \pi^+}$	165415	1129780	1347574
$(p_0')^2$	159376	1089159	1303793
$p_</p_>$	105002	809107	972315
p_t	102007	782256	960263
α		18.43%	11.65%

Table 8: Number of data and Monte Carlo signal events after each cut.

7 Analysis of Selected Events

The purpose of this analysis is the measurement of the BR($K_S \to \pi^{\pm} e^{\mp} \nu_e$) and the mass difference $\Delta m = m_{K_L} - m_{K_S}$ using K_{e3} decays.

As it was shown in Section 2.5.3, assuming the validity of the $\Delta S = \Delta Q$ rule and the CPT theorem, and neglecting any CP violation effect, the decay rates of both K_{e3} charge modes can be expressed like:

$$N^{+} = S^{+}(p) \cdot \left[\eta^2 e^{-\Gamma_S t} + e^{-\Gamma_L t} + 2 \cdot e^{-(\Gamma_L + \Gamma_S)t/2} \cdot \eta D(p) \cdot cos(\Delta m \cdot t)\right],$$

$$N^{-} = S^{-}(p) \cdot \left[\eta^2 e^{-\Gamma_S t} + e^{-\Gamma_L t} - 2 \cdot e^{-(\Gamma_L + \Gamma_S)t/2} \cdot \eta D(p) \cdot cos(\Delta m \cdot t)\right], \tag{7.1}$$

with

$$\begin{aligned} \eta &= \frac{\langle \pi^{\mp} e^{\pm} \nu_e | H | K_S \rangle}{\langle \pi^{\mp} e^{\pm} \nu_e | H | K_L \rangle}, \\ S^{\pm}(p) &= N(K^0) + N(\overline{K^0}), \\ D(p) &= \frac{N(K^0) - N(\overline{K^0})}{N(K^0) + N(\overline{K^0})}. \end{aligned}$$

The ± signs in $S^{\pm}$ account for possible different global normalization constants in both decay modes.

From the fit of equations (7.1) to the corresponding true lifetime distributions of the selected K_{e3} data, both η and Δm can be obtained. Using the information from the magnet spectrometer the reconstruction of the z-decay vertex position is possible. A transformation of true lifetime distributions into reconstructed z-decay vertex distributions or vice-versa is first needed.

- **The Unfolding Method**

  With an ideal detector, one could measure the lifetime of every single event and any $f(t)$ could be obtained by a simple histogram of this time measurement. With real detectors the determination of $f(t)$ is complicated by three effects:

  Limited Acceptance

The probability to observe a given event, the detector acceptance, is less than 1, resulting in a certain loss of recorded events. The acceptance depends on the lifetime and energy of the decaying particle.

Transformation

Instead of the lifetime t, the measured quantity is the z-decay vertex position. The relation between t and z is given by a Lorentz transformation between the lab frame and the particle's rest frame. This transformation depends on the energy of the decaying particle, which cannot be fully reconstructed due to the uncertainty in the energy of the neutrino.

Finite Resolution

The measured quantity, the z-decay vertex position is smeared out due to the finite resolution of the detector. Thus there is a statistical relation between the time of flight of the particle and its z-decay vertex position.

Mathematically, the relation between the theoretical distribution $f(t)$ and the measured one, $\mathcal{F}(z)$, is given by the integral of

$$d\mathcal{F}(z) = A(t, z)f(t)dt, \tag{7.2}$$

where $A(t, z)$ is the resolution function and contains all the effects of limited acceptance, transformation and resolution of the detector. For a given value $t = t_0$ the resolution function $A(t_0, z)$ describes the response of the detector in the variable z for that fixed value t_0. The problem to determine the distribution $f(t)$ from a measured distribution $f(z)$ is called 'unfolding' whereas the opposite operation is called 'folding'.

In order to find a numerical solution for equation (7.2), the distributions can be represented by histograms and in that case the resolution function is represented by a matrix. The equation

$$\vec{z} = A \cdot \vec{t} \tag{7.3}$$

has to be solved for the vector $\vec{t}$, given the vector $\vec{z}$. The vector $\vec{z}$ with n-elements represents a histogram of the measured quantity z, and the distribution $f(t)$ is represented by a histogram of vector $\vec{t}$ with m-elements. The elements of these vectors are bin contents. The transformation from t to z is described by the n-by-m matrix A. The element a_{ij} is related to the probability to observe an entry in histogram

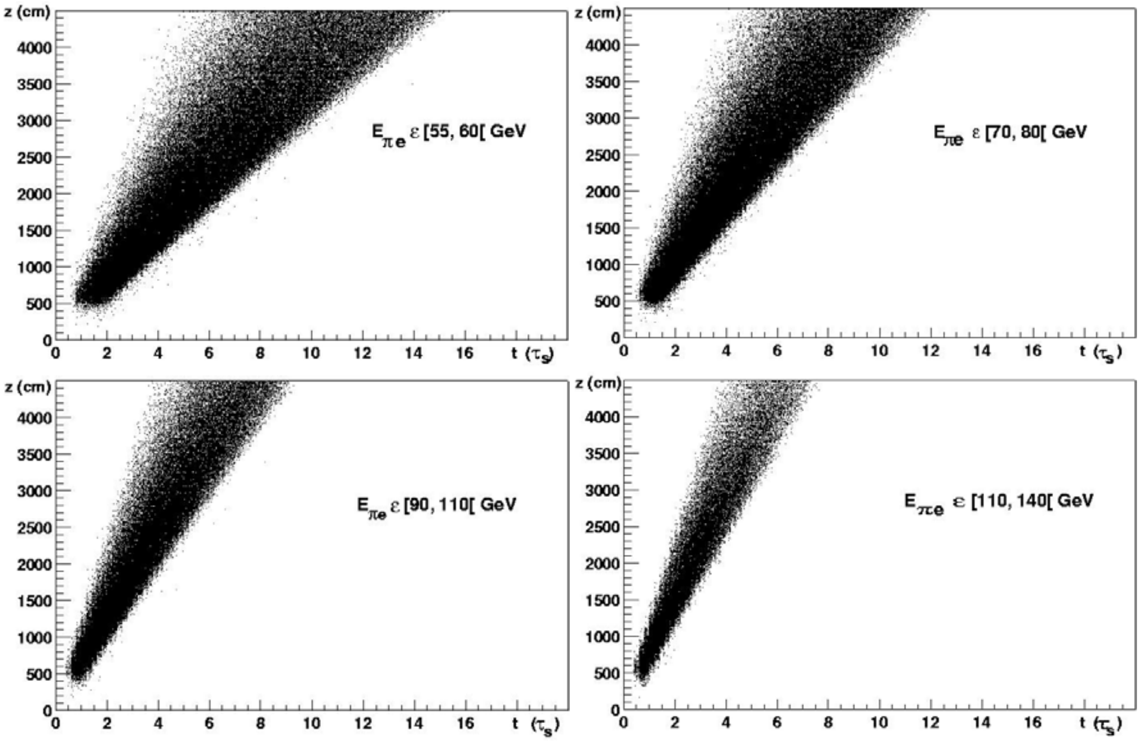

Figure 37: Resolution matrices for different energy bins. True lifetime vs reconstructed z-decay vertex position of selected Monte Carlo K_{Le3}-events.

bin i of the histogram z, if the true value t comes from histogram bin j of the histogram t of the true values.

In Monte Carlo simulations, both the true and the reconstructed values are accessible for the generated variables. The resolution matrix A can therefore be obtained directly from Monte Carlo simulations.
More information about unfolding methods can be found in ref [37].

7.1 The Fit

This analysis is performed in bins of energy. Differences in the variation of the reconstructed energy spectrum between data and simulated Monte Carlo events can be neglected as long as the acceptance variation within the energy bins is sufficiently small. A variable bin size of 5 to 30 GeV is chosen to keep those differences in the acceptance as low as possible while accepting a similar amount of events within each one of the energy bins.

The different $A(E)$ matrices for the different energy bins can be obtained from the simulation of uniformly distributed K_{e3}- decays. Since both K_{Le3}- and K_{Se3}-decays are kinematically equivalent and the only difference between them arises from the probability distributions, $d^2N/dzdE$ (eq (5.2)), the acceptances of both decays as a function of the energy and the z-decay vertex position are exactly the same for both decays. As a consequence, and since the fit to the data is performed in bins of energy and z, it is possible to use only one kind of MC K_{e3}-events to obtain the resolution matrices. In order to cover a wider range of lifetimes and z-decay vertex positions with the need of much less statistics, the Monte Carlo simulation of K_{Le3}-decays is chosen for this purpose (see Figure 37). There is no need to consider different $A^{\pm}(E)$ matrices for the positive and negative charge decay modes because both decays suffer the same processes at the energies considered in this experiment and therefore the acceptances and resolution effects are practically the same for both modes.

In order to achieve a reasonable resolution, a binning of 100 bins in $\vec{z}$ and $\vec{t}$ is chosen. Statistical fluctuations coming from finite Monte Carlo samples may be neglected if the Monte Carlo sample is much larger than the data sample. It is assumed that a factor of 10 in the size of the Monte Carlo sample compared to the data is large enough.

Depending on the energy of the pion-electron system, a folding is applied to equations (7.1) in order to express them as a function of the z-decay vertex position. A gaussian contribution, $g(E)$, is then added to the result of the folding operation. This gaussian contribution (see Section 6.2.6) is used to account for the remaining low-p_t events which come from the scattering of particles at the collimator, and it is defined like:

$$g(E) = (H_{high\ p_t}(E) \cdot k) \cdot e^{-\frac{(z-573)^2}{2 \cdot 143^2}}, \tag{7.4}$$

where the mean and width, $\mu = 573$ cm and $\sigma = 143$ cm, do not depend on the energy bin and are obtained from the mean of the gaussian fits to the high-p_t events, $H_{high\ p_t}(E)$ is height resulting also from the same gaussian fits, and k is the ratio between the number of low-p_t events and the number of high-p_t events of a given energy bin. The assumption here is that this ratio is constant and does not depend on the energy bin which is considered.

After adding the background contribution to the result of the matrix multiplication, the fit to the data is performed. A fit depending on the energy and z-decay vertex position is done simultaneously for the decay distributions of the two different charge modes. A total of 14 different distributions, two per bin of energy, are fitted at the same time with 24 free parameters:

- 14 different global normalization constants depending on the energy bin and the charge decay mode: $N^{\pm}(E)$,
- 7 different dilution factors depending on the energy of the decay products: D(E),
- the mass difference: $\Delta m = m_{K_L} - m_{K_S}$,
- the η factor: $\eta = \frac{\langle \pi^{\mp} e^{\pm} \nu_e | H | K_S \rangle}{\langle \pi^{\mp} e^{\pm} \nu_e | H | K_L \rangle}$ and
- a global constant k proportional to the number of remaining background events.

The Minuit minimization package [38] is used to search for the minimum of the χ^2 function. The kaons lifetimes are fixed parameters of the fit and take the values published in ref [3], $\tau_S = (0.8935 \pm 0.0008) \times 10^{-10}$s and $\tau_L = (5.17 \pm 0.04) \times 10^{-8}$s.

7.2 Results of the Fit

The results of the fit for Δm and η are:

$$\begin{aligned} \Delta m &= (0.443 \pm 0.039\ _{(\mathrm{stat})})\ \hbar \tau_S^{-1} \\ \eta &= 0.903 \pm 0.039\ _{(\mathrm{stat})} \end{aligned}$$

$$\chi^2/\mathrm{ndof} = 1089/1040$$

which corresponds to a probability of 14.2% in the quality of the fit.
A summary of the results of the fit for all the parameters can be found in Table 9. The variation of the dilution factor (introduced in Section 2.5.3) as a function of the energy of the pion-electron system can also be seen in Figure 38.
The fit is performed for the energy bins shown in this table and between $z \ \epsilon \ [600, 4000]$ cm. The results from the fit to each one of the z-decay vertex distributions can be seen in Figures 39 and 40.

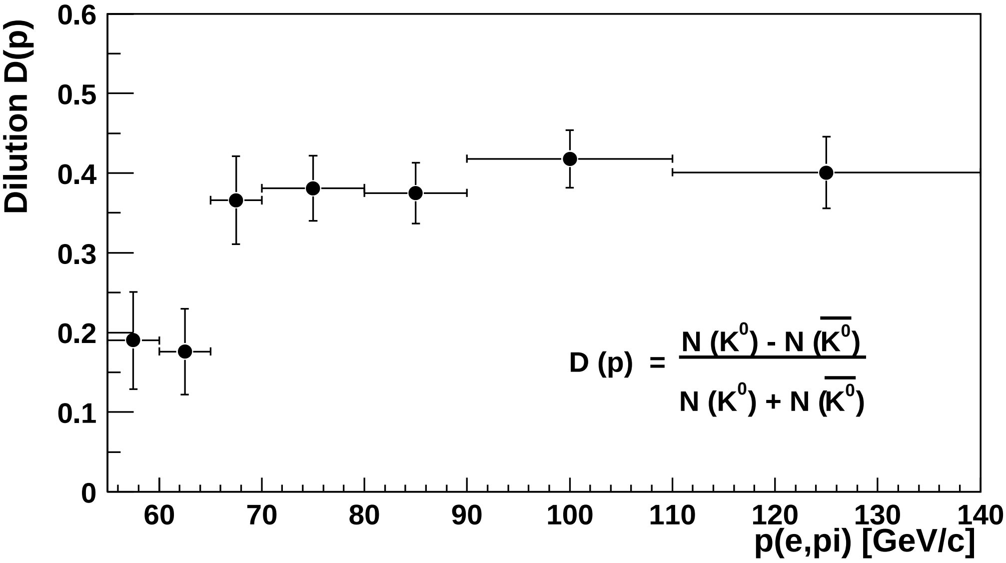

Figure 38: Variation of the dilution factor as a function of the energy of the pion-electron system. Only statistical errors are shown.

Energy (GeV)	Parameter	Value ± Error	Energy (GeV)	Parameter	Value ± Error
55 - 60	S^+	0.952 ± 0.013	80 - 90	S^+	0.884 ± 0.016
	S^-	0.955 ± 0.013		S^-	0.980 ± 0.017
	D	0.190 ± 0.061		D	0.375 ± 0.038
60 - 65	S^+	0.934 ± 0.014	90 - 110	S^+	0.834 ± 0.016
	S^-	0.953 ± 0.014		S^-	0.980 ± 0.020
	D	0.176 ± 0.054		D	0.418 ± 0.036
65 - 70	S^+	0.924 ± 0.016	110 - 140	S^+	0.780 ± 0.020
	S^-	0.984 ± 0.017		S^-	0.970 ± 0.028
	D	0.366 ± 0.055		D	0.401 ± 0.045
70 - 80	S^+	0.912 ± 0.015	55 - 140	Δm	$0.442 \pm 0.039\ \hbar\tau_S^{-1}$
	S^-	0.972 ± 0.015		η	0.903 ± 0.039
	D	0.381 ± 0.041		k	0.86 ± 0.23 cm

Table 9: Results of the fit. Only statistical errors are shown.

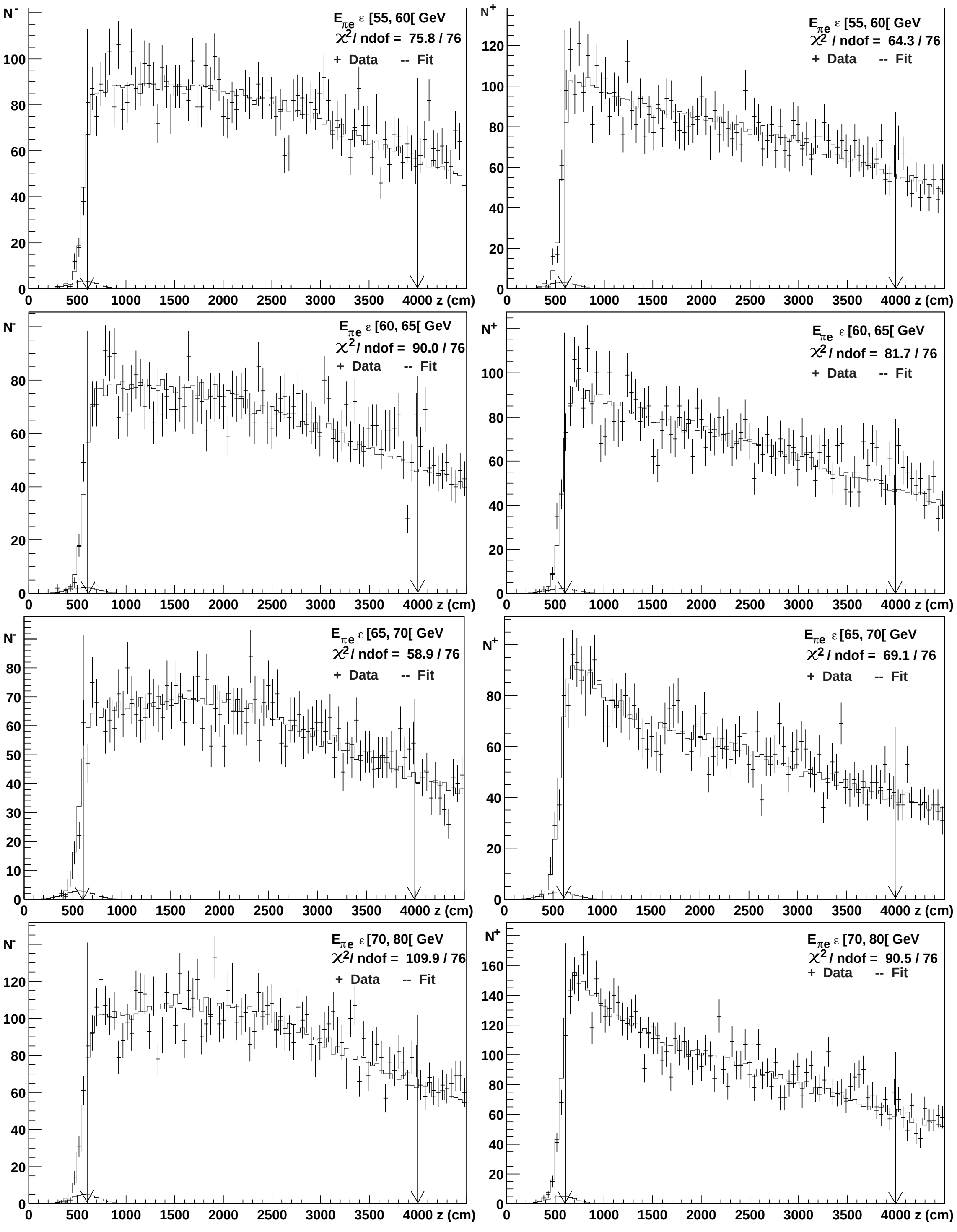

Figure 39: Results of the fit to the z-decay vertex distributions of the two charge decay modes for the different bins of energy. The arrows mark the z-region in which the fit was performed. The expected remaining gaussian contribution coming from the scattering of particles at the collimator is also shown and included in the fit.

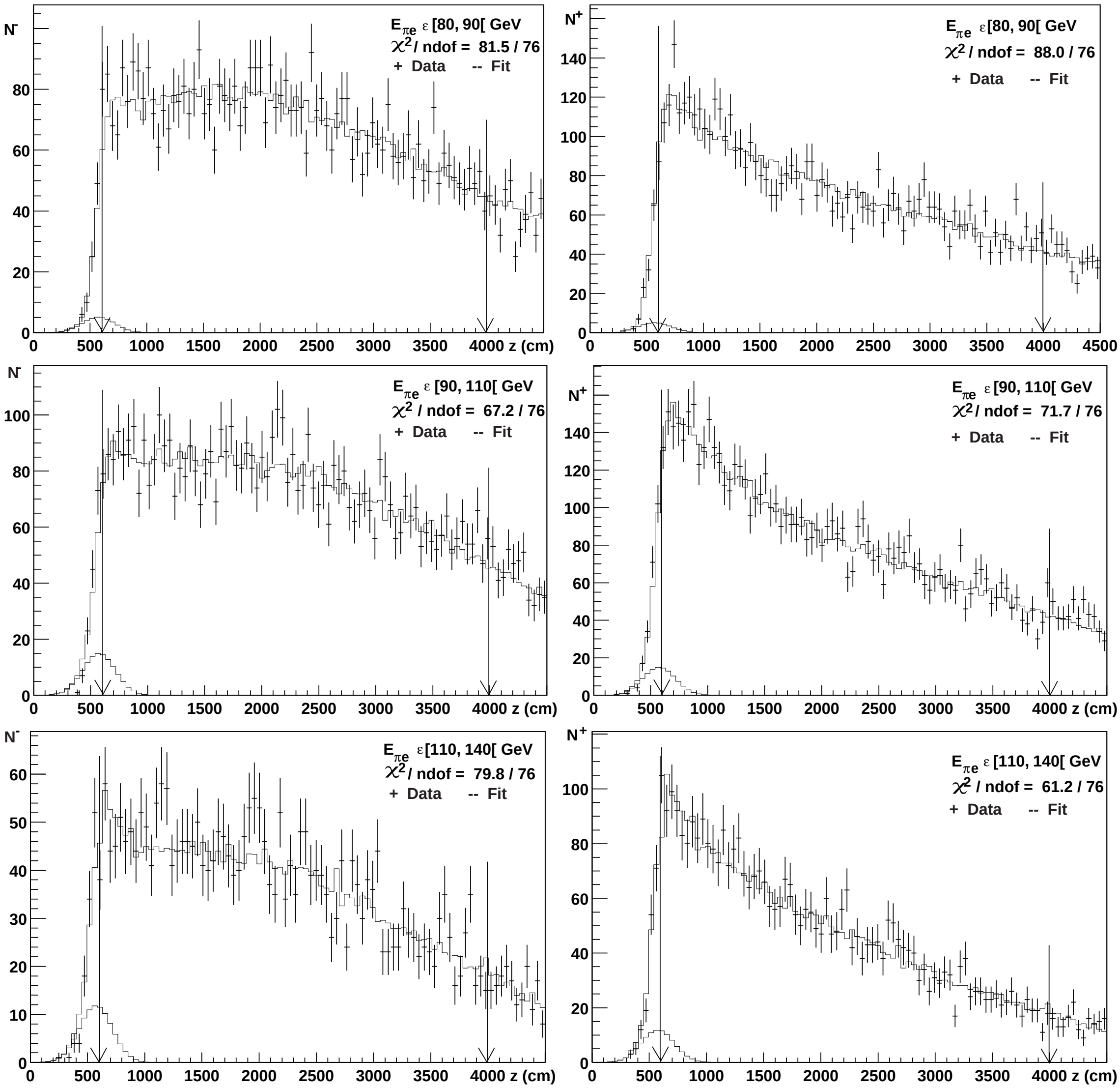

Figure 40: Results of the fit to the z-decay vertex distributions of the two charge decay modes for the different bins of energy. The arrows mark the z-region in which the fit was performed. The expected remaining gaussian contribution coming from the scattering of particles at the collimator is also shown and included in the fit.

Assuming the validity of the $\Delta S = \Delta Q$ rule and the CPT theorem then $\eta = 1$ in eqs (7.1). The result for the mass difference fixing η to 1 and fitting under the same conditions is:

$$\Delta m = (0.425 \pm 0.038\ _{\mathrm{(stat)}})\ \hbar\tau_S^{-1}$$

$$\chi^2/\mathrm{ndof} = +1096/1041$$

Repeating the fit with Δm fixed to its tabulated value:
$\Delta m = (0.5300 \pm 0.0012) \times 10^{10}\hbar s^{-1}$ [3], gives:

$$\eta \;\; = \;\; 0.894 \pm 0.042\ _{\mathrm{(stat)}}$$

$$\chi^2/\mathrm{ndof} = 1090/1041$$

These results are in very good agreement with the measurement presented in this section both in the case of Δm and η, and this is due to the very small correlation between these parameters.

7.3 Systematic Uncertainties

Systematic uncertainties in the measurement of Δm and η can arise from several sources.

The Analysis Cuts

The distributions of some variables can have strong variations within the region in which the cut on them is applied. Changing the limits of these cuts can alter the value of the measurement and therefore be a source of systematic uncertainties.

In Table 10 the main cuts which can contribute to the systematic uncertainty of the measurement are listed together with the new cutting limits and the corresponding results for Δm and η obtained with them.
The systematic uncertainties due to each cut can be in found in Table 11. These uncertainties are calculated by choosing the largest variation on the results produced by each cut. The final systematic uncertainty is calculated by adding in quadrature these variations depending on their relative sign.
As can be seen from Table 11, the systematic uncertainty on Δm is negligible compared to the statistical one. On the contrary, the systematic uncertainty on η is larger than the statistical one and arises mainly from the variation of the limits of the EOP and the transverse momentum cuts. The reason for this large uncertainty is the high correlation between η and the normalization constants of the fitted distributions. By varying the EOP and p_t cuts, the

selected final data sample is allowed to include more background events or to reject good K_{e3}-events. In both cases, both the normalization constants and η are strongly affected by the change on the number of selected events.

An improvement of the systematic uncertainty on η is possible if a term which can account properly for the excess of background events due to the widening of the cuts is included in the fit. A complete understanding of the scattering of particles at the collimator would make possible a more reliable fit in the low τ_S region where there is a clean contribution of η^2.

Cut	$\Delta m \pm \delta(\Delta m)$ $(\hbar\tau_S^{-1})$	$\eta \pm \delta\eta$
$cda < 2.2$ cm	0.443 ± 0.039	0.901 ± 0.039
$cda < 2.8$ cm	0.442 ± 0.039	0.904 ± 0.039
$0 < EOP\|_\pi < 0.85$ $0.9 < EOP\|_e < 1.1$	0.437 ± 0.024	0.943 ± 0.036
$0 < EOP\|_\pi < 0.75$ $1.0 < EOP\|_e < 1.1$	0.440 ± 0.064	0.966 ± 0.072
$d_{tracks} > 5$ cm	0.443 ± 0.039	0.904 ± 0.039
$d_{tracks} > 9$ cm	0.442 ± 0.039	0.903 ± 0.039
$(p_0')^2 < -0.005$ (GeV/c)^2	0.439 ± 0.039	0.908 ± 0.039
$(p_0')^2 < -0.015$ (GeV/c)^2	0.442 ± 0.040	0.898 ± 0.041
$p_</p_> > 0.39$ (GeV/c)	0.438 ± 0.039	0.911 ± 0.039
$p_</p_> > 0.41$ (GeV/c)	0.440 ± 0.040	0.913 ± 0.039
$p_t < 0.16$ (GeV/c)	0.441 ± 0.041	0.869 ± 0.043
$p_t < 0.24$ (GeV/c)	0.443 ± 0.039	0.939 ± 0.038

Table 10: Change in Δm and η due to variations of cutting limits.

Cut	$\Delta_{syst}(\Delta m)$ $(\hbar\tau_S^{-1})$	$\Delta_{syst}(\eta)$
cda	0.001	-0.005
EOP	0.006	-0.067
d_{tracks}	0.001	-0.005
$(p_0')^2$	0.004	$-0.009 \quad +0.001$
$p_</p_>$	0.003	-0.014
p_t	0.002	$-0.040 \quad +0.030$
Systematic Uncertainty	0.008	$-0.080 \quad +0.030$

Table 11: Systematic uncertainties due to variations of cutting limits of analysis cuts.

The Fit

The result may also change if the parameters of the fit are varied. In order to evaluate the possible uncertainties due to the fitting procedure, several parameters of the fit are varied here. In Table 12 the change in the results produced by the variation of different parameters is listed. The parameters which are varied here are the z-decay vertex fitting region, the gauss parameters used to account for the collimator scattering and the binning of the distributions.

Fit	$\Delta m \pm \delta(\Delta)$ $(\hbar\tau_S^{-1})$	$\eta \pm \delta\eta$
z ϵ $[500, 4000]$ cm	0.437 ± 0.040	0.871 ± 0.05
z ϵ $[800, 4000]$ cm	0.464 ± 0.036	0.860 ± 0.038
gauss parameters: $\mu = 515$ cm, $\sigma = 118$ cm	0.442 ± 0.038	0.920 ± 0.035
50 bins distributions	0.439 ± 0.039	0.865 ± 0.039

Table 12: Changes in Δm and η due to variation of fit parameters.

A summary of the systematic uncertainties arising from the variations of the fitting parameters can be in found in Table 13. The final systematic uncertainty is calculated by adding in quadrature all the contributions. As can be seen from this table, the systematic uncertainty on Δm due to the fit is negligible compared to the statistical one. The systematic uncertainty on η is of the order of the statistical one. A better simulation of the collimator scattering inside the fit would decrease this uncertainty giving a cleaner contribution of η in the low z-decay vertex regions.

Fit	$\Delta_{syst}(\Delta m)$ $(\hbar\tau_S^{-1})$	$\Delta_{syst}(\eta)$
z-fitting region	-0.021 +0.006	+0.039
gauss parameters	+0.001	-0.021
50 bins distributions	+0.004	+0.034
Systematic Uncertainty	-0.021 +0.0072	-0.021 +0.052

Table 13: Systematic uncertainties due to variation of fit parameters.

The Monte Carlo Simulation

Monte Carlo simulations tend to overestimate the accuracy with which the detector can measure and reconstruct the variables. In order to account for this effect, an additional resolution of 10% on the reconstructed z-decay vertex position of each event is added to the Monte Carlo. In Table 14 the results from this check and the systematic uncertainty obtained from it are listed.

Monte Carlo	$\Delta m \pm \delta(\Delta m)$ $(\hbar\tau_S^{-1})$	$\eta \pm \delta\eta$
additional 10% resolution in z	0.446 ± 0.039	0.910 ± 0.039
Systematic Uncertainty	-0.003	-0.011

Table 14: Systematic uncertainty due to resolution effects of the Monte Carlo.

In Table 15 all the contributions to the systematic uncertainties on the measurement of Δm and η are listed. The final value of the uncertainty is given in the last line of the table and is computed by adding in quadrature the former values depending on their relative sign.

Source of Systematic Uncertainty	$\Delta_{syst}(\Delta m)$ $(\hbar\tau_S^{-1})$	$\Delta_{syst}(\eta)$
Analysis Cuts	+0.0081	-0.080 +0.030
Fit	-0.021 +0.0072	-0.021 +0.052
Monte Carlo	-0.003	-0.011
Systematic Uncertainty	-0.021 +0.011	-0.083 +0.060

Table 15: Summary of all systematic uncertainties.

7.4 Final Results

The final results of Δm and η are:

$$\begin{aligned}\Delta m &= (0.443 \pm 0.039\ _{\text{(stat)}}\ {}^{+0.011}_{-0.021}\ _{\text{(syst)}}) \quad \hbar\tau_S^{-1},\\ \eta &= 0.903 \pm 0.039\ _{\text{(stat)}}\ {}^{+0.083}_{-0.060}\ _{\text{(syst)}},\end{aligned}$$

where the first contribution to the error is given by the statistical error of the measurement and the last one is due to systematics.

From the measurement of η it is possible to obtain $\Gamma(K_S \to \pi^\pm e^\mp \nu_e)$ and $\mathrm{BR}(K_S \to \pi^\pm e^\mp \nu_e)$:

$$\eta^2 = \frac{\langle \pi^\mp e^\pm \nu_e | H | K_S \rangle^2}{\langle \pi^\mp e^\pm \nu_e | H | K_L \rangle^2} = \frac{\Gamma(K_S \to \pi^\mp e^\pm \nu_e)}{\Gamma(K_L \to \pi^\mp e^\pm \nu_e)}, \tag{7.5}$$

and therefore,

$$\Gamma(K_S \to \pi^\mp e^\pm \nu_e) = \eta^2 \cdot \Gamma(K_L \to \pi^\mp e^\pm \nu_e). \tag{7.6}$$

Since

$$\mathrm{BR}(K_{S,L} \to \pi^\pm e^\mp \nu_e) = \frac{\Gamma(K_{S,L} \to \pi^\mp e^\pm \nu_e)}{\Gamma(K_{S,L} \to \mathit{all})} = \frac{\tau_{S,L} \cdot \Gamma(K_{S,L} \to \pi^\mp e^\pm \nu_e)}{\hbar}, \tag{7.7}$$

substituting eq (7.6) into eq (7.7):

$$\mathrm{BR}(K_S \to \pi^\pm e^\mp \nu_e) = \frac{\eta^2 \cdot \tau_S \cdot \mathrm{BR}(K_L \to \pi^\pm e^\mp \nu_e)}{\tau_L}. \tag{7.8}$$

Substituting $\tau_{S,L}$, $\Gamma(K_L \to \pi^{\pm}e^{\mp}\nu_e)$ and $\mathrm{BR}(K_L \to \pi^{\pm}e^{\mp}\nu_e)$ in the previous expressions with their current accepted values (ref [3]): $\tau_S = (0.8935 \pm 0.0008) \times 10^{-10}$ s, $\tau_L = (5.17 \pm 0.04) \times 10^{-8}$ s, $\Gamma(K_L \to \pi^{\pm}e^{\mp}\nu_e) = (7.50 \pm 0.08) \times 10^6\ s^{-1}$ and $\mathrm{BR}(K_L \to \pi^{\pm}e^{\mp}\nu_e) = (38,78 \pm 0.28)\%$, the following results are obtained:

$$\boxed{\begin{array}{ccc}
\Delta m & = & (0.443 \pm 0.039\ _{\text{(stat)}}\ ^{+0.011}_{-0.021}\ _{\text{(syst)}})\ \hbar\tau_S^{-1} \\[1em]
\Gamma(K_S \to \pi^{\mp}e^{\pm}\nu_e) & = & (6.06 \pm 0.53\ _{\text{(stat)}}\ ^{+1.12}_{-0.81}\ _{\text{(syst)}}) \times 10^6\ \mathrm{s}^{-1} \\[1em]
\mathrm{BR}(K_S \to \pi^{\pm}e^{\mp}\nu_e) & = & (5.31 \pm 0.46\ _{\text{(stat)}}\ ^{+0.98}_{-0.71}\ _{\text{(syst)}}) \times 10^{-4}
\end{array}}$$

8 Conclusions and Outlook

In this work $K_{S,L} \rightarrow \pi^{\pm}e^{\mp}\nu_e$ decays were analyzed. A measurement of the mass difference between the K_L- and the K_S-meson in neutral kaons semielectronic decays was presented here. Using the same data sample, the direct measurement of the branching ratio $\mathrm{BR}(K_S \rightarrow \pi^{\pm}e^{\mp}\nu_e)$ was also possible.

8.1 Conclusions

The value for the mass difference $\Delta m = m_{K_L} - m_{K_S}$ obtained from this analysis is:

$$\boxed{\begin{aligned} \Delta m &= (0.443 \pm 0.039\ _{(\mathrm{stat})}\ {}^{+0.011}_{-0.021}\ _{(\mathrm{syst})})\quad \hbar\tau_S^{-1} \\ &= (0.496 \pm 0.044\ _{(\mathrm{stat})}\ {}^{+0.012}_{-0.024}\ _{(\mathrm{syst})}) \times 10^{10}\ \hbar\mathrm{s}^{-1} \end{aligned}}$$

The current world's average result of Δm is:

$$\Delta m = (0.5300 \pm 0.0012) \times 10^{10}\ \hbar\mathrm{s}^{-1}[3], \tag{8.1}$$

and it was obtained from different measurements performed before July 2000.

The resolution of the measurement presented here is 9% and it differs from the world's average value in less than one standard deviation. The uncertainty of this result is dominated by the statistical error of the measurement and therefore it can be improved by increasing the amount of statistics.

Assuming the validity of the $\Delta S = \Delta Q$ rule and the CPT theorem, the prediction for the decay width $\Gamma(K_S \rightarrow \pi^{\pm}e^{\mp}\nu_e)$ was quoted to be:

$$\Gamma(K_S \rightarrow \pi^{\pm}e^{\mp}\nu_e) \quad = \quad (7.50 \pm 0.08) \times 10^6 \ s^{-1} \qquad [39]. \qquad (8.2)$$

This prediction was published in 1998 and was using previous results of $\Gamma(K_L \rightarrow \pi^{\pm}e^{\mp}\nu_e)$ measurements and assuming $\Gamma(K_L \rightarrow \pi^{\pm}e^{\mp}\nu_e) = \Gamma(K_S \rightarrow \pi^{\pm}e^{\mp}\nu_e)$.

Using the NA48 detector a direct measurement of the decay width $\Gamma(K_S \rightarrow \pi^{\pm}e^{\mp}\nu_e)$ has been possible by studying the interference between K_S-K_L semieletronic decays. The result from this analysis is:

$$\boxed{\Gamma(K_S \rightarrow \pi^{\pm}e^{\mp}\nu_e) = (6.06 \pm 0.53 \ _{\text{(stat)}} \ ^{+1.12}_{-0.81} \ _{\text{(syst)}}) \times 10^6 \ \text{s}^{-1}}$$

which is equivalent to a branching ratio of:

$$\boxed{\text{BR}(K_S \rightarrow \pi^{\pm}e^{\mp}\nu_e) = (5.31 \pm 0.46 \ _{\text{(stat)}} \ ^{+0.98}_{-0.71} \ _{\text{(syst)}}) \times 10^{-4}}$$

The uncertainty of this measurement is dominated by systematic effects. This uncertainty can be eliminated after a deep understanding and simulation of the scattering of particles at the K_S collimator of the NA48 detector.

The most precise measurement of this branching ratio is:

$$\text{BR}(K_S \rightarrow \pi^{\pm}e^{\mp}\nu_e) \quad = \quad (6.91 \pm 0.37 \ _{\text{(stat)}}) \times 10^{-4} \qquad [2]. \qquad (8.3)$$

where the experiment was using for this purpose tagged K_S decays produced in $e^+e^- \rightarrow \Phi \rightarrow K_S K_L$ collisions.

Considering only the contribution of the statistical error to the $\Gamma(K_S \rightarrow \pi^{\pm}e^{\mp}\nu_e)$ measurement, the resolution presented here is 9%. This resolution is already comparable to the 5% resolution achieved by the DAPHNE collaboration [2] and can improve it by at least a factor 25 by using the data sample that is expected to be available at the end of this year.

8.2 Outlook

The 100000 K_{e3} events used for this analysis were selected from the data sample collected during the 48 hours of data taking of the named '1999 K_S High Intensity Run'.

In October 2001 a second K_S high intensity run was performed. From this period it is expected to extract about 800000 K_{e3}-events after all selection cuts, which means 8 times more events than the amount used here.

From the middle of June until the middle of September 2002 the NA48 experiment will have a whole K_S High Intensity Run period in which approximately 6×10^7 K_{e3}-events are expected to be collected.

This huge amount of statistics can be translated into a great improvement of the resolution of the measurements of both the mass difference $\Delta m = m_{K_L} - m_{K_S}$ and the branching ratio BR($K_S \rightarrow \pi^\pm e^\mp \nu_e$). In the case of BR($K_S \rightarrow \pi^\pm e^\mp \nu_e$) where the error is currently dominated by systematics, an increase of the amount of statistics would permit a better understanding and simulation of collimator scattering effects, and therefore a much more accurate measurement. Table 16 summarizes the possible improvement of the resolution of these measurements using data collected in different run periods. Only statistical errors have been considered in this table.

	NA48 1999	World Average	NA48 2001	NA48 2002
$\frac{\delta(\Delta m)}{\Delta m}$	9%	0.25%	3%	0.3%
$\frac{\delta(BR(K_{Se3}))}{BR(K_{Se3})}$	8.6%	5%	3%	0.3%

Table 16: Possible improvements in the measurement of Δm and η

References

[1] R. Akhmetshin *et al.*, Phys. Lett. B456 (1999) 90.

[2] A. Aloisio *et al.*, Phys. Lett. B525, 37 (2002).

[3] D. E. Groom, *et al.* Eur. Phys. J. C15, 1-878 (2000).

[4] M.K. Gaillard, P.D. Grannis, F.K. Sciulli, The Standard Model of Particle Physics, Rev. Mod. Phys. 71:596-5111 (1999).

[5] G. Lüders. Ann. Phys., 2 (1957).

[6] W. Pauli, Niels Bohr and the development of Physics, McGraw Hill, 1955.

[7] T.D. Lee, C.N. Yang, Phys. Rev. 104, 254 (1956).

[8] C.S. Wu, E. Ambler, R. W. Haywarth, D.D. Hoppes, and R.P. Hudson, Phys. Rev., 105: 1413 (1957).

[9] J.H. Christenson, J.W. Cronin, V.L. Fitch, R. Turlay, Phys. Rev. Lett. 13, 138 (1964).

[10] A. Lai *et al.*, Eur. Phys. Journal C22, 231-254 (2001).

[11] R. Batley *at al.*, A precision measurement of direct CP violation in the decay of neutral kaons into two pions, CERN-EP-2002-061, hep-ex/0208009 , Subm. to: Phys. Lett. B (2002).

[12] T.D. Lee, C.S. Wu, Ann. Rev. Nucl. Sci. 16, 511 (1966).

[13] Gaillard *et al.*, Comment on calculation of the $K_L \rightarrow \mu\, \overline{\nu}_\mu$ decay rate and the $K_L\, K_S$ mass difference in Gauge theories. Phys.Rev. D13, 2674 (1976).

[14] N. Cabibbo, Phys. Rev. Lett. 10, 531 (1963).

[15] A. García, P. Kielanowski, The Beta Decay of Hyperons, Springer Verlag, Berlin, New York (1985).

[16] E. Fermi, Z. Physik 88, 161 (1934).

[17] K. Kleinknecht, Ann. Rev. Nucl. Sci., 26: 1-50 (1976).

[18] A. Angelopoulos, *et al.* Measurement of the $K_L - K_S$ mass difference using semileptonic decays of tagged neutral kaons, Phys. Lett., B444: 38-42 (1998).

[19] J.A. Graham, Measurement of the direct CP-violating parameter $\mathrm{Re}(\varepsilon'/\varepsilon)$ and the kaon sector parameters ΔM, τ_S and $\Phi_{\pm}$, PhD Thesis, Chicago (2001).

[20] R. Carosi *et al.*, Phys. Lett., B237: 303-312 (1990).

[21] V. Fanti *et al.*, Phys. Lett. B465, 335 (1999).

[22] G. Barr *et al.*, NA48 proposal - CERN SPSC 90-22 and SPSLC P253, The beam and detector for a precision CP violation experiment NA48, (1990).

[23] A.J. Buras, M. Ciuchini, E. Franco, G. Isidori, G. Martinelli, and L. Silvestrini, Final State Interactions and $\frac{\varepsilon'}{\varepsilon}$: A Critical Look, Phys. Lett. B480: 80-86 (2000).

[24] L. Masetti, Ricerca del dicadimento $K_S \to \pi^0\gamma\gamma$, Ferrara (2000).

[25] Sven A. Schmidt, Die Zerfallsasymmetrie des radiativen Hyperonzerfalls $\Xi^0 \to \Lambda\gamma$, Dissertation, Mainz (2002).

[26] B. Hay, R. Moore, I. Wingerter, Compact User's Guide, CERN (1999).

[27] J. Schmidt, Bestimmung des Verhältnisses $\frac{\Gamma(K_L \to \pi^{\pm}\mu^{\mp}\nu_{\mu})}{\Gamma(K_L \to \pi^{\pm}e^{\mp}\nu_e)}$, Dissertation, Mainz (1997).

[28] R. Brun and F. Rademakers, The ROOT System Home Page, http://root.cern.ch, CERN (2000).

[29] K. Talleur, Messung der Verzeigungsverhältnisse $\Xi^0 \to \Lambda\gamma$ und $\Xi^0 \to \Sigma^0\gamma$, Diplomarbeit, Mainz (2000).

[30] M. Debeer *et al.*, NASIM User's Guide, Saclay (1996).

[31] Application Software Group, GEANT, Detector Description and Simulation Tool, CN Division, CERN (1994).

[32] H. Blümer, H. Rohrer, NMC User's Guide, Mainz (1991).

[33] J. Schmidt, V. Schönharting, NMC User's Guide, NA48 Note 96-17 (1996).

[34] H. W. Atherton *et al.*, Precise Measurement of Particle Production by 400 GeV Protons on Beryllium Targets, CERN Yellow Report 80-07 (1980).

[35] U. Koch, Messung der radiativen Hyperon-Zerfälle $\Xi^0 \to \Sigma^0\gamma$ und $\Xi^0 \to \Lambda\gamma$ und Präzisionsmessung der Ξ^0-Masse mit dem NA48-Detektor, Dissertation, Mainz (1998).

[36] U. Koch, Personal Communication, Mainz (2001).

[37] V. Blobel, An unfolding method for high energy physics experiments, Contribution to the Conference: Advanced Statistical Techniques in Particle Physics, Durham, 18 - 22 March (2002).

[38] Application Software Group, MINUIT -Function Minimization and Error Analysis, Version 94.1, Computing and Networks Division, CERN (1994).

[39] D. E. Groom, *et al.* Eur. Phys. J. C15, 1 (1998).

List of Figures

List of Tables

Acknowledgements

First of all I sincerely would like to thank Prof. Dr. K. Kleinknecht for giving me the chance of joining this working group and for his support during the last year.

I would like to thank Dr. Carmen García and Dr. Rainer Wanke for their continuous interest, support and for making this thesis possible.

I am especially grateful to Prof. Dr. A. Ferrer for introducing me to Prof. Dr. K. Kleinknecht and also to Prof. Dr. J. Bernabéu for his friendly and useful talks at CERN.

In addition I want to thank all the members of the WA ETAP. They have contributed a lot to this thesis with many discussions. Especially I want to mention the 3 Andis, Lucia, Irakli, Paulo, Matthias, Martin, Uli, Sven, Peter, Michael, Kirsten and Silvia. I hope I did not forget anyone.

Jens Oster, Tristán Valenzuela, Uwe Koch and Esteban Fullana: thank you very much for your constant help.

A mis amigos María, Loli, Paco, Mónica, Vicente (Bata) y a toda la familia de Mainz quiero darles las gracias por ayudarme y animarme siempre.

A mis padres, Pilar y Manolo, a mis abuelos, Cristina, José, Rosario y Manolo, a mi hermana, María, a Rogelio y a toda mi familia quiero agradecerles su amor y apoyo incondicional. Os quiero mucho.

Finalmente y muy en especial, quiero dedicar esta tesina a mi abuela Cristina, Sol, a quien tanto adoro, admiro y añoro.